Optimisation and Characterisation of Heusler Alloy CoCrFeAl for Spin Hall devices

Tiffany Sarfo

Master of Science (by Research)

Physics

May 2023

Abstract

As humanity becomes more reliant on technology, it is important look into the development of more efficient technology. This is essential in sustaining technological process. Electron spin is an underutilised property that an emerging technology called spintronics aims to exploit in order to advance memory storage.

This study seeks to investigate optimise quaternary Heusler alloy CoCrFeAl for spin Hall application. CoCrFeAl is a class of Heusler alloys referred to as spin gapless semiconductors. The unique band structure makes it an alloy of interest. In this study CoCrFeAl of thickness 200 Å is fabricated by sputtering and characterised chemically, structurally and magnetically. In addition, a CoCrFeAl Hall bar of thickness 200 Å capped with 20 Å of Pt is fabricated to measure the spin Hall effect. Annealing temperatures and growth conditions were found to impact the crystallinity and magnetisation of CoCrFeAl. This study found that CoCrFeAl deposited by sputtering crystallised in at least *A2* type ordering and can reach nearly 100% of its theoretically calculated magnetic saturation value of 784 emu/cm^3. It also displays the spin Hall effect with spin Hall angle of 0.019.

Acknowledgements

Declaration

I declare that the work presented in this project is based purely on my own research unless otherwise stated and has not been submitted for a degree in either this or any other university.

Introduction

Aim

The purpose of this research is to optimise and investigate quaternary CoCrFeAl Heusler alloy for spin Hall devices. Thin films were deposited by HiTUS sputtering. The thin film samples are then characterised chemically by energy dispersive X-ray (SEM-EDX), structurally by X-Ray diffraction (XRD) and magnetically by vibrating sample magnetometer (VSM) In this study, samples are optimised by doping and *ex-situ* annealing. The four-point probe method is used to investigate spin Hall properties of CoCrFeAl.

Outline

Chapter 1 provides the theoretical background of the project by introducing the concept of magnetoresistance and its different types as well as real world applications. Following this, a brief overview of spintronics in provided to understand the relevant spin transport property of this study and its applications. This leads into an area of interest within spintronics – Heusler alloys. The development of Heusler alloys for spintronic applications is discussed in this section before narrowing the scope to spin-gapless semiconducting CoCrFeAl which is the Heusler alloy of interest.

Chapter 2 gives an in-depth overview of the experimental methods used in this study.

Chapter 3 presents the results acquired whilst attempting to optimise the growth of CoCrFeAl films. This section will discuss the growth conditions and annealing temperatures used and give a more in-depth analysis of the CoCrFeAl thin films fabricated in this study. An attempt at measuring the spin Hall effect is presented in this section.

The final section of this thesis concludes this project and presents possible avenues for future studies.

Table of Contents

1. Background

1.1 Magnetoresistance

Magnetoresistance describes the phenomenon where the electrical resistance of a material can be changed by applying a magnetic field to it. In 1856, William Thomson first discovered magnetoresistance by placing iron in a magnetic field and observed that when the current was in the same orientation of the magnetic field, the resistance of the iron would increase and the resistance would decrease when the current was in an orientation perpendicular to the magnetic field [1].

There are many different types of magnetoresistance, such as giant magnetoresistance [2] and tunnelling magnetoresistance [3].

1.1.1 Anisotropic Magnetoresistance

Anisotropic Magnetoresistance (AMR) is observed in ferromagnetic materials. Thomson's experiment with iron demonstrated anisotropic magnetoresistance. He repeated the same experiment with nickel and observed the same phenomenon that had occurred in iron but to a stronger magnitude [1].

AMR is observed when there is a change in material resistivity due to its orientation in a magnetic field. The angular dependency of resistivity can be defined with the following equation:

$$\rho(\theta) = \rho_\perp + (\rho_\parallel - \rho_\perp) \cos^2(\theta) \tag{1.1}$$

where $\rho_\perp$ and $\rho_\parallel$ are the resistivity when the magnetic field is perpendicular and parallel to the current respectively. The anisotropic magnetoresistance occurs due to spin-orbit coupling; when the magnetic field is applied, it influences the spin of electrons which then impacts the scattering of electrons. This leads to a change of resistance as a result of the difference of collisions of electrons depending on the direction of the magnetic field.

1.1.2 Giant Magnetoresistance

In 2007, the Nobel prize in Physics was awarded to Peter Grünberg and Albert Fert for their work in documenting the giant magnetoresistance effect (GMR) [3]. GMR was discovered simultaneously and independently by Grünberg *et al.* [2] and Fert *et al.* [4] in 1988. GMR was initially observed in a structure that consisted of a non-magnetic metal sandwiched by ferromagnetic as seen in *Figure 1.1*. GMR is dependent on the spin dependent scattering of a material so the GMR structure was designed in a way to exploit this by expanding on previous experiment conducted by Mott in 1936 [5] who discovered that it is possible for current to be separated by two spin channels in a transition metal.
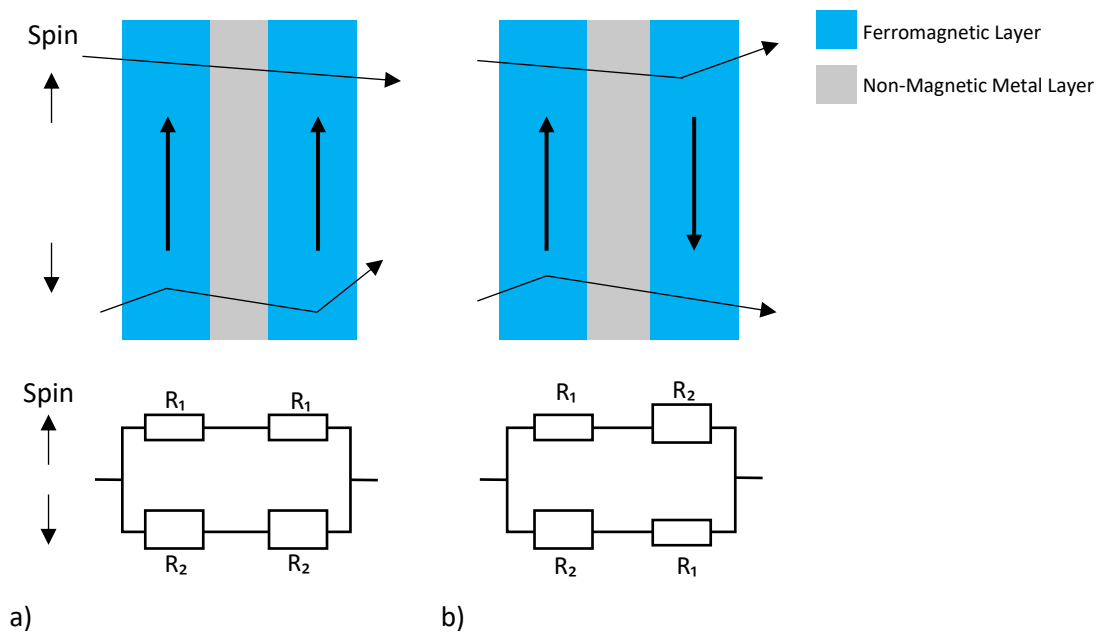
Figure 1.1: Schematic diagram of the Mott model where the a) parallel and b) anti-parallel configuration in the structure where GMR is observed.

According to the Mott model. GMR can be represented as a parallel resistor network as shown in *Figure 1.1.* In this model, the ferromagnetic layers acts as resistors with different resistivities in a parallel and anti-parallel configuration. When the magnetic moments of the ferromagnetic layers are aligned in parallel (P), there is a small resistance produced due to little or no spin scattering occurring. Conversely, when the magnetic moment of the two ferromagnetic

layers are aligned in anti-parallel (AP) configuration, the resistance is comparably larger due to strong spin scattering.

This can be expressed mathematically as:

$$R_{\text{P}} = \frac{2R_1 + R_2}{R_1 + R_2} \text{ and } R_{\text{AP}} = \frac{R_1 + R_2}{2} \qquad \text{(1.2 and 1.3)}$$

where R_{P} and R_{AP} represents *Figures 1.1a and 1.1b* respectively.

Equation 1.2 and *1.3* can be used to define the GMR ratio:

$$\text{GMR ratio} = \frac{\Delta R}{R} = \frac{R_{\text{AP}} - R_{\text{P}}}{R_{\text{P}}} = \frac{(R_1 - R_2)^2}{4R_1 R_2} \qquad \text{(1.4)}$$

The principle of GMR was used by IBM to produce hard disk drive (HDD) read head [6].

1.1.3 Tunnelling magnetoresistance

Tunnelling magnetoresistance (TMR) is principally similar to GMR. Where in GMR, the two ferromagnetic layers sandwich a non-magnetic metal layer, in TMR the sandwiched material is an insulator. This phenomenon was discovered by Michel Julliére in 1975 [3].

Figure 1.2: Schematic diagram of DOS of ferromagnetic layers that experience the TMR effect [7].

The probability of electrons tunnelling through the insulator barrier is higher when the magnetic moments are aligned in parallel 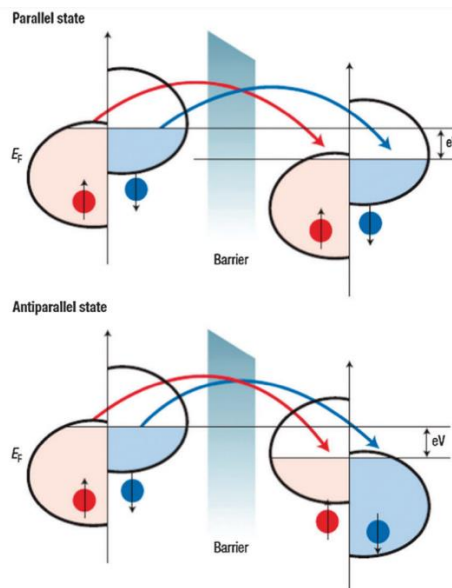due to the presence of an applied magnetic field; in this configuration the two ferromagnetic layers have the same density of states which results in a low resistance. In an anti-parallel configuration, there is a difference at the Fermi level due to the differences in the density of states (DOS). This results in a high resistance because the difference in the DOS between the ferromagnetic layers lowers the probability of electrons tunnelling through the insulator layer as there may be no states available for electron to tunnel through to.

The TMR ratio can be expressed mathematically as:

$$\text{TMR ratio} = \frac{\Delta R}{R} = \frac{R_{\text{AP}} - R_{\text{P}}}{R_{\text{P}}} = \frac{2P_1 P_2}{1 - P_1 P_2} \tag{1.5}$$

where P_1 and P_2 refers to the spin polarisations of the two ferromagnetic layers. The spin polarisation can be expressed as

$$P = \frac{N_{\text{majority}} - N_{\text{minority}}}{N_{\text{majority}} + N_{\text{minority}}} \tag{1.6}$$

where N_{majority} and N_{minority} refer to the number of electrons in the majority and minority spin channels at the Fermi energy level respectively, as indicated by the DOS of the ferromagnetic layers.

1.1.4 Magnetic Random Access Memory

Magnetic Random Access Memory (MRAM) is a non-volatile memory that utilises the TMR effect to store data. Data storage is reliant on magnetisation, not charge carriers like other conventional random access memories such as DRAM and SRAM (dynamic random access memory and static random access memory respectively).
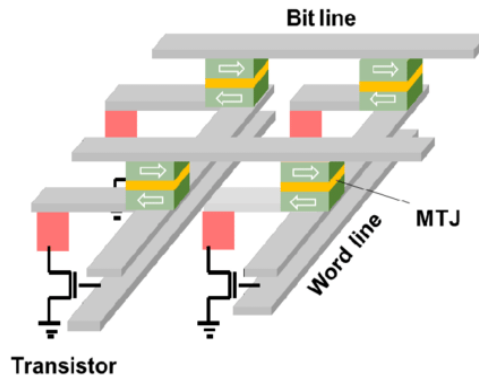
Figure 1.3: Simplified schematic of MRAM [8].

In MRAM, the data is stored in the ferromagnetic layer of an MTJ cell and a transistor is used to read and write data.

Data is stored using logic binary '0' and '1'. A current is applied along the bit and word lines that generate a magnetic field which can cause a change in the magnetisation of one of the layers in the MTJ cell because the other ferromagnetic layer is fixed. If the magnetisation in both ferromagnetic magnetic layers align, then the MTJ cell is in the parallel configuration which has low resistance and corresponds with binary state '0'. If the magnetic moments are in the anti-parallel configuration, then there is a high resistance which corresponds with binary '1'.

Although the MRAM is still an emerging technology with more research currently being conducted in order for it to be widely commercially available [9], it has the potential to revolutionise data storage by replacing conventional random access memory technology.

1.2 Spintronics

Moore's law predicted that the number of transistors on microchips doubles every two years [10]. This has been the trend since 1965, but is becoming obsolete as transistors reach their physical limit in terms of size. Therefore, it is important that we look into quantum alternatives. Spintronics is a field where

the intrinsic properties of an electron, called spin, is used in electronic devices. Spintronics is a portmanteau of spin electronics.

Iridium manganese (IrMn) is a popular alloy used in spintronics. This poses a problem because iridium is a rare-earth metal element. The development of new storage technologies, such as new generation hard disk drives and MRAM, has lead to an increase in the demand for iridium compounds over the past decades. More recently, a sharp increase in the price of iridium can be attributed to the COVID-19 pandemic [11] and an increase in demand of use of iridium as catalyst for green technology [12]. One candidate material to replace iridium in spintronic devices is Heusler Alloys [13] which are later discussed in section 1.3.
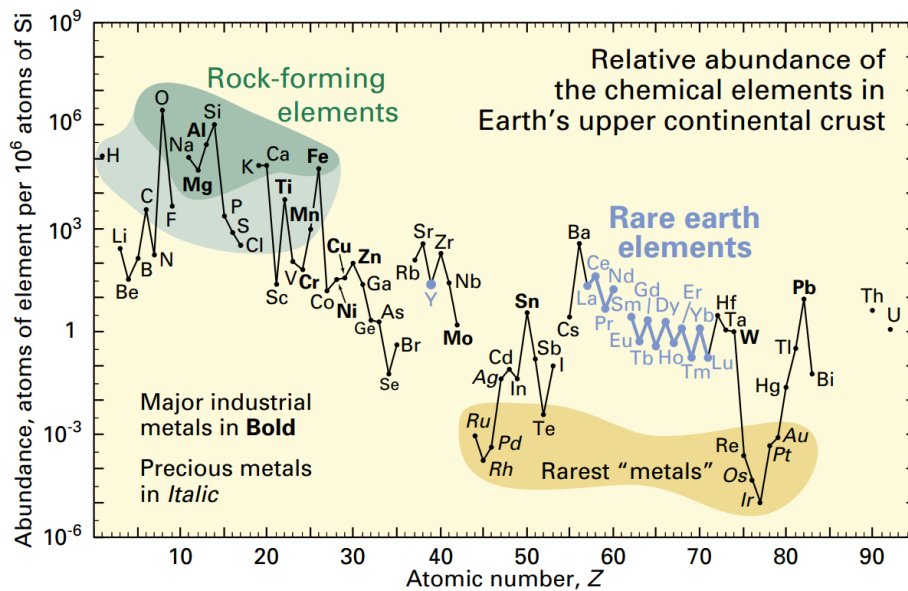
Figure 1.4: The abundance of different elements in the crust of the earth [14].

Given that iridium is a rare-earth metal element, it would not be wise to depend on it as a future alternative. Heusler alloy based Spintronic devices are a promising alternative as they are theoretically more efficient than traditional electronic devices due to high spin polarisation [15]. This means that spintronics could lead to a more sustainable solution to making digital devices in addition to advancing technology further by utilising electron spin.

1.2.1 Spin Hall effect

The spin Hall effect is a spin transport phenomenon that was first theoretically proposed by Mikhail Dyakonov and Vladimir Perel in 1971 [16]. In 1999, the first spin Hall experimental procedure to detect the spin Hall effect was proposed by Jorge Hirsch [17] and Zhang [18] and was first experimentally observed by Sinova *et al.* in 2004 [19].
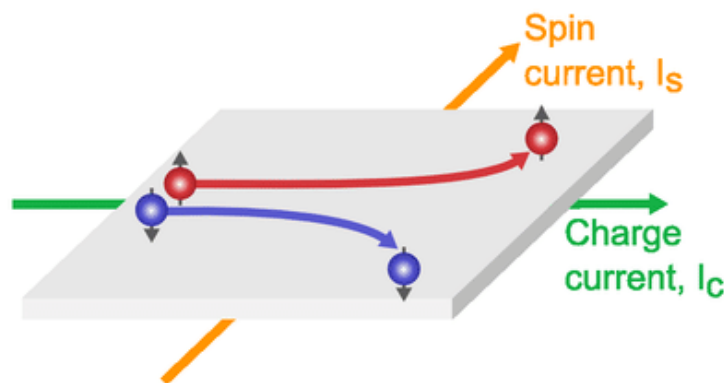
Figure 1.5: A schematic diagram of the spin Hall effect [20].

When a charge current is introduced to a material, it can cause spin polarisation to occur within the material. This results in the spin up and spin down electrons accumulating on adjacent sides of a material perpendicular to the direction of the charge current flow. This effect is analogous with the classic Hall effect [21].

The spin Hall angle is a ratio that quantifies the spin Hall effect and describes how efficient a material is at producing a spin Hall current. For this study, Pt was used as the spin Hall bar capping layer due to its strong spin orbit coupling properties.

1.3 Heusler Alloys

Heusler alloys are named after chemist Fritz Heusler, who discovered Heusler alloys at the beginning of the twentieth century. Heusler discovered that an alloy Cu_2MnAl exhibited ferromagnetic behaviour despite the constituent materials – copper, manganese and aluminium being non-magnetic elements

[22]. Today, Heusler alloys refers to a class of ternary or quaternary compounds, that have face centred cubic (fcc) crystal structure and have magnetic properties. Ternary Heusler alloys can be further divided into two subclasses; half Heusler alloys and full Heusler alloys. Heusler alloys can be made with nearly every element in the periodic table as seen in *Figure 1.6*.

Figure 1.6: Periodic table showing which elements can be in a Heusler alloy [23].

As a result, there are over 3000 known Heusler alloys which makes this class of materials incredibly versatile. This diversity in properties is why Heusler alloys are alloys of great interest in spintronics due to their half-metallic properties which is later discussed in *Section 1.3.3*. Quaternary Heusler alloy CoCrFeAl is investigated in this study.

1.3.1 Crystal Structure in Heusler Alloys

The most common crystal structure of Heusler alloys is the fcc unit cell structure which comprises of eight corner atoms and six face centred atoms, resulting in four atoms per unit cell.

Heusler alloys have stoichiometry 1:1:1 for half Heusler alloys and 2:1:1 for full Heusler alloys. Ternary Heusler alloy compounds can be denoted by XYZ and X_2YZ respectively, where X and Y are transition metal elements and Z is a main group element. Quaternary Heusler alloys, sometimes referred to as equiatomic quaternary Heusler alloys, have a stoichiometry of 1:1:1:1 which is denoted as XX'YZ. Quaternary Heusler alloys are similar to full Heusler but differs in atomic composition as one of the X atoms is substituted with a different transition metal element. Quaternary Heusler alloys usually belong to space group F-43 no. 216.

In quaternary Heusler alloys, the Wyckoff positions are occupied by the four different elements; 4a (0,0,0), 4b (½ , ½, ½) , 4c (¼ , ¼ , ¼) and 4d (¾ , ¾ , ¾) and can be configured into three different crystal structure configurations as seen in *Figure 1.7*. In type I, the X and Y elements occupy the Wyckoff position 4c and 4d respectively. In type II, the two X and X' transition elements occupy positions 4c and 4d respectively and in type III, X' and Y occupy position 4c and 4d.

a)   b)   c)
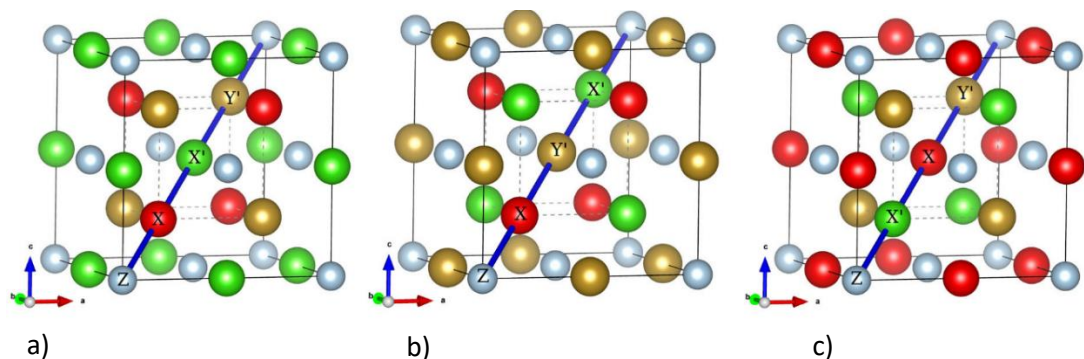
Figure 1.7: Schematic diagram of a) type I, b)type II and c) type III crystal structure configurations of quaternary Heusler alloys [24].

Whereas configuration type refers to the specific arrangement of atoms in a unit cell unit, there is also the possibility of disorder within the crystal structure which can impact the property of a Heusler alloy. Disorder describes the deviation of a crystal structure from its ideal configuration. An ideal configuration implies a perfectly ordered crystal structure which is the fully ordered $L2_1$ structure. Other configurations can be classified into different types

of disorder with the most commonly known being $A2$, $B2$ and $D0_3$. $A2$ type disorder describes the intermixing of the four elements in all Wyckoff positions. $B2$ type disorder describes the intermixing of Y and Z atomic lattice sites, resulting in a Cs-Cl structure. X element atoms remain in the centre of the structure in this type of disorder. $D0_3$ disorder type describes intermixing of the X atomic lattice site with either X or Y atoms, resulting in a BiF_3-type structure. This type of disorder is the rarest out of the previously mentioned disorder types.
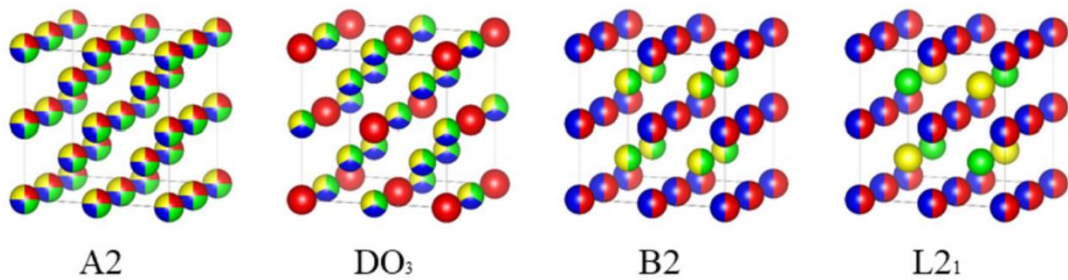
Figure 1.8: Schematic diagram of different type of crystal disorder [25].

1.3.2 Magnetic Ordering

Heusler alloys exhibit a range of magnetic behaviour such as ferromagnetic [26], paramagnetic [27] and antiferromagnetic behaviour [28]. The crystal structure and composition play a large role in the magnetic properties.

The magnetic moments of constituent atoms within a unit cell also impacts the magnetic properties of a Heusler alloy. The crystal structure is made up of sub lattices, with each atom possessing a different amount of magnetic moments.

The structural disorder also influences magnetic moment. For example, a Heusler alloy with the $L2_1$ structure in a ferromagnetic phase follows the generalised Slater-Pauling behaviour whereas a disordered phase may not.

1.3.3 Half-metallicity

Half-metallicity is a property present in some ferromagnetic Heusler alloys. Half metallicity describes the property of having two spin band structures within a

material. A spin band refers to the energy states of electrons in a specific spin direction; spin up or spin down. In a half-metallic material, the Fermi level of the minority spin channel is located within the bandgap and is semiconducting. The majority spin channel is a metallic material. In the spin band structure of a half-metallic Heusler alloy, the density of states for the minority spin channel drops to zero at the Fermi level. The asymmetry of this structure, as shown in *Figure 1.8*, results in the material where it is conductive in one spin direction and acts almost as an insulator in the other direction. This property is highly desirable for spintronics devices because of its capability for 100% spin polarisation.
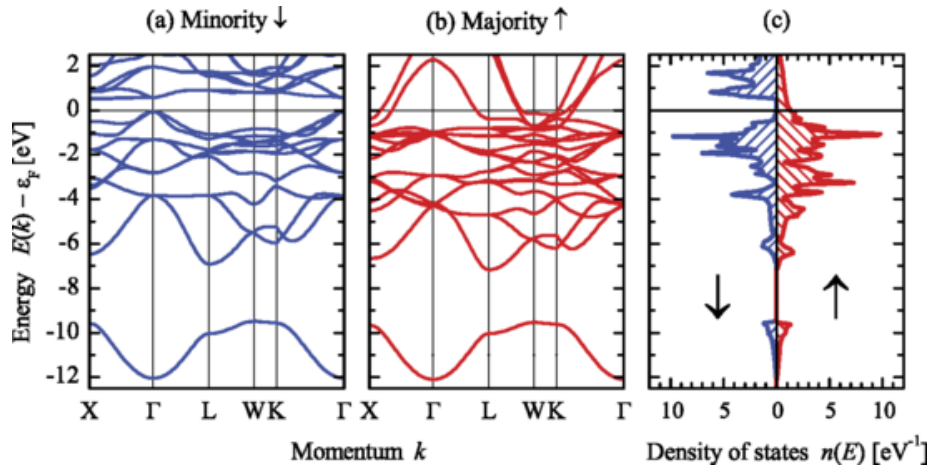
Figure 1.8: Schematic diagram of the theoretical bandgap of half-metallic material [29].

A Heusler alloy must adhere to the Slater-Pauling rule in order to show half-metallicity [30]. The generalised Slater-Pauling rule stems from the work done on ferromagnetism by Slater [31] and Pauling [32] in the 1930s to predict the magnetic moment of compounds that contain transition metals. They discovered that the electron in the $3d$ orbital influenced a material's ferromagnetism as it is the only orbital shell where spin up and spin down electrons are not all paired.

The generalised Slater Pauling rules can be written as [30]:

$$M_t = N_V - 24 \tag{1.7}$$

where M_t is the total spin magnetic moment and N_V is the total number of valence electrons.
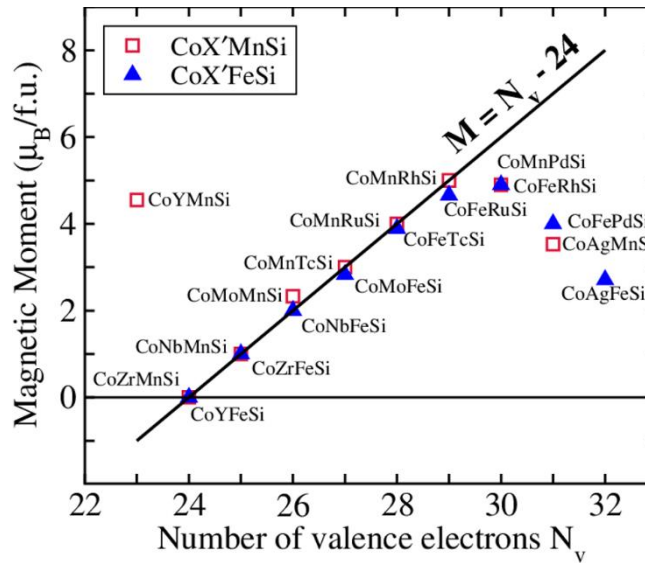
Figure 1.9: A graph showing the relationship generalised Slater-Pauling rule for a range of Co-based quaternary Heusler alloys [33].

The Slater-Pauling rule is a powerful tool in the study of half-metallic materials as it allows for the theorisation of new Heusler alloys with half-metallic properties by substituting X, Y or Z.

1.3.4   Band Gap

A band gap refers to the difference in energy levels between the valence band, the energy band where electrons are bound to an atom, and the conduction band, the energy band where electrons can flow.

The band gap of a material is a crucial in understanding the properties of a material as it determines the electrical characteristics of the material. For example, a material with a wide band gap at the Fermi level does not conduct electricity well as there are not many states available near the Fermi energy level. The closer the Fermi level is to the conduction band energy, the easier it will be for electrons in the valence band to transition into the conduction band. This is due to the high amount of energy needed to excite electrons from the highest energy level in a valence band into the lowest energy level of the conduction band. In contrast, a semiconductor material with a narrow bandgap

conducts electricity more easily because less energy is needed in order to excite electrons from the valence band into the conduction band. As a result, materials with wide band gap are usually indicative of insulators whereas materials with a narrow band gap are indicative of a semiconductor material. As shown in *Figure 1.10*, conductors possess an even smaller band gap than semiconductors.
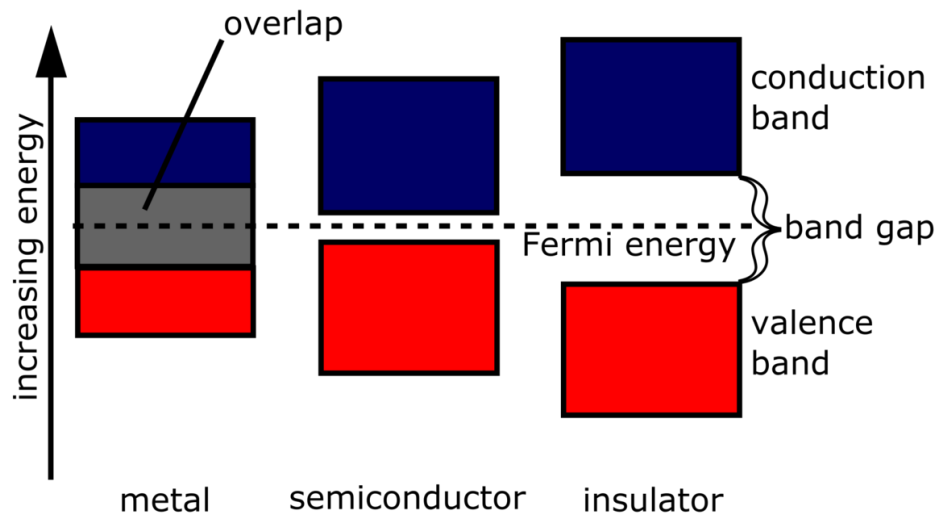
Figure 1.10: Schematic diagram showing the typical band structure of insulator, semiconductor and conducting metal. Each band contains density of states [34].

In Heusler alloys, it is possible to tune the bandgap by changing the composition of an alloy [13]. The band gap is defined by the DOS in a material; the DOS refers to the number of different available electronic states an electron is allowed to occupy at a given energy level. It is directly related to the electronic structure of the material as DOS can be used to describe how many electronic states are distributed within an energy band.

Tuning a Heusler alloy by changing its composition would make it possible to shift the DOS to near the Fermi level, hence altering its electronic properties.

1.3.5 Cobalt-based Heusler alloys

The spin moments of valance electrons that are localised to the d orbitals of the Co atoms is what determines the magnetic moment in Co-based Heusler alloys [35]. This stems from the complex hybridisations of the atomic orbitals. The

band structure of a cobalt-based Heusler alloy can be changed by varying the local hybridization.

Cobalt based Heusler alloys gained attention after Ishida *et al.* proposed full Heusler alloys Co₂Mn(Z) (Z = Ge, Si) as a half-metallic ferromagnets [36] which was elaborated on by Galanakis *et al.* [37]. *Figure 1.11* shows how Galanakis *et al.* conceptualised and calculated interactions of Co-Co atoms. Galanakis study used Co₂Mn(Z), (Z = Si or Ge) which showed that Mn and Co hybridised in a similar manner to Co-Co [37]. This is possible because all elements in a Heusler alloy have *s*, *p* and *d*-orbitals. For X, Y and Z, the *s* and *p*-orbitals sit below the Fermi level, resulting in only the *d*-orbital state influencing band structure. Transitional metal X, in this case Cobalt and Manganese, are the only element within the structure with *d*-orbital states capable of hybridisation. As a result, the interaction between cobalt and manganese frees five hybridised orbitals leading to a gap in the minority spin channel.
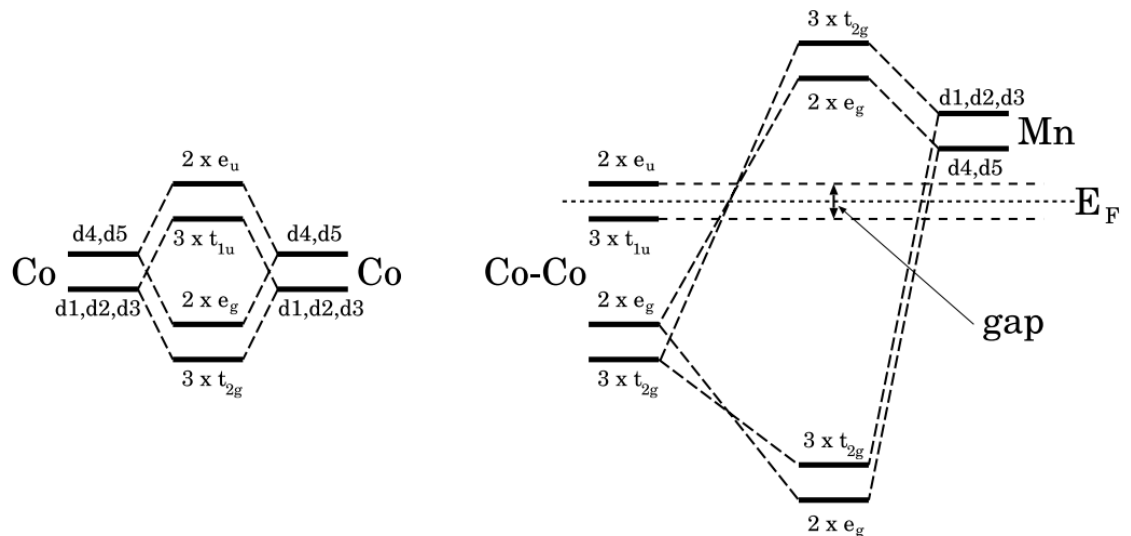
Figure 1.11: Schematic illustration of the origin of the gap in the minority band in full-Heusler alloys [37].

This shows that it is possible that the DOS at the Fermi level can be increased by doping a Co-based Heusler alloy with cobalt or another transition metal element atoms to increases the number of 3*d* orbital states available. This can lead to a narrowing of the band gap (and subsequently half-metallic properties).

Cobalt-based Heusler alloys can be either ternary or quaternary Heusler alloys, depending on the number of atoms in the unit cell. Some well-known Heusler alloys that have cobalt as one of its constituent elements are Co_2MgGe as well as Co_2MnSi[38] and Co_2FeSi[39], and Co_2CrAl[40], which have been extensively studied.

Cobalt-based Heusler alloys are of particular interest for spintronics and other applications due to their unique electronic and magnetic properties. Some of the interesting properties of cobalt-based Heusler alloys include:

1. High Curie temperature: Cobalt-based Heusler alloys are suitable to use at high temperatures due to having a high Curie temperature. The Curie temperature of a materials refers to the temperature at which it demagnetises [41].

2. High spin polarisation: Cobalt-based Heusler alloys can theoretically possess 100% spin polarisation at the Fermi level [42].

3. Large magnetoresistance: Cobalt-based Heusler alloys have a high magnetoresistance, meaning that a change in magnetic field causes a change in resistance [43]. Heusler alloys with higher saturation magnetisation are preferable for spintronics because it results in strong spin accumulation. This allows for more stable magnetism. Stability of magnetic states is important as it makes devices, such as MRAM [44], less susceptible to external magnetic fields.

Overall, Heusler alloys have shown promising results in improving the performance of spintronic devices, particularly in terms of reducing the power consumption and increasing the efficiency of these devices due to increased magnetic stability and increase spin polarisation respectively.

1.3.6 Spin polarisation

Spin polarisation is a measure of the degree to which the spin-up and spin-down electronic states are separated in a material.

In Co-based Heusler alloys, the Co atoms have a partially filled $3d$ electronic shell, which results in the magnetic moment. Due to the crystal structure and electronic configuration of the alloy, the magnetic moments of the Co atoms align in a particular direction, resulting in a net magnetic moment for the entire crystal. This magnetic ordering leads to a spin polarisation effect in which the majority and minority spin states are shifted in energy with respect to each other.

The spin polarisation can be quantified by the spin polarisation ratio, which is the ratio of the difference in the DOS at the Fermi level between the majority and minority spin states to the total DOS at the Fermi level.

1.3.7 Spin Gapless Semiconductors

Spin gapless semiconductors (SGS) are materials that possess no band gap for one spin channel and a finite band gap for the other spin channel [45]. In spin gapless semiconductors, there is no band gap which results in little to no energy required to excite electrons from the valence band to the conduction band. In addition, excited electrons have 100% spin polarisation. This unique band structures makes spin gapless semiconductors ideal for spintronic applications.
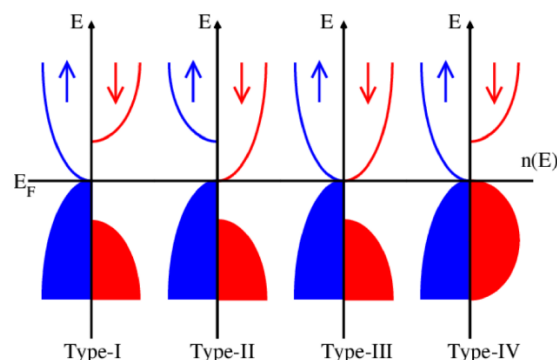
Figure 1.12: Schematics of these four SGS types, where blue is the majority band gap and red is the minority band gap [46].

In SGSs, the generalised Slater-Pauling rule is also satisfied [47] and the lack of band gap makes SGSs more preferable for spintronic applications than half-metallic ferromagnets as it allows for more tuneable spin transport devices. SGSs have the potential to be more efficient as the minimal threshold energy required leads to 100% spin polarisation occurring further than in half-metallic metals which is particularly useful for data storage spintronic devices [45].

However, a disadvantage of SGSs is that it is sensitive to change of chemical composition or crystal structure. This can lead to a loss in half-metallic behaviour which is not ideal. Design and fabrication of SGSs needs to be done carefully in order to achieve a material with the desired properties.

1.3.8 CoCrFeAl

CoCrFeAl Heusler alloy has attracted the interest of spintronic research in recent years [24],[50],[51]. This is due to CoCrFeAl being a cobalt-based Heusler alloy that is also a spin gap-less semiconductor. The combination of traits makes CoCrFeAl a potentially promising material because it has the potential for 100% spin polarisation. A material like this would be ideal for spintronic applications to allow for more efficient devices.

Before the proposal of spin gapless semiconductors, *Gao et al.* first designed and proposed quaternary Heusler alloy CoCrFeAl by first principles calculations [50]. After the proposal of spin gapless semiconductors, Xu *et al.* identified CoCrFeAl as a spin gapless semiconductor and conducted further first principles studies and concluded CoCrFeAl was a promising candidate for spintronic devices because it obeyed the Slater-Pauling rule [51]. This was further supported by *ab-initio* electronic structure calculations by Özdogan *et al.* which predicted a lattice constant of 5.70 Å [48].

Limited experimental research has been conducted with CoCrFeAl. Most research study bulk CoCrFeAl which is made through the process of arc melting which may be different to properties of epitaxial CoCrFeAl grown from sputtering at room temperature because the alloy already exposed to high temperatures during deposition [52–54]. A recent study by *Chen et al.* in 2022,

investigated sputtered CoCrFeAl on a MgO substrate [55] which provides useful insights into sputtered CoCrFeAl but substrate can have an impact on lattice structure so it is important to consider whether depositing on CoCrFeAl on Si may yield different results as small changes in crystal structure can have an impact on the corresponding properties.

2. Methods

2.1 Sample Preparation

2.1.1 High Target Utilisation System

Thin film samples were fabricated using a High Target Utilisation Sputtering system (HiTUS), manufactured by Plasma Quest Ltd.

a)   b)
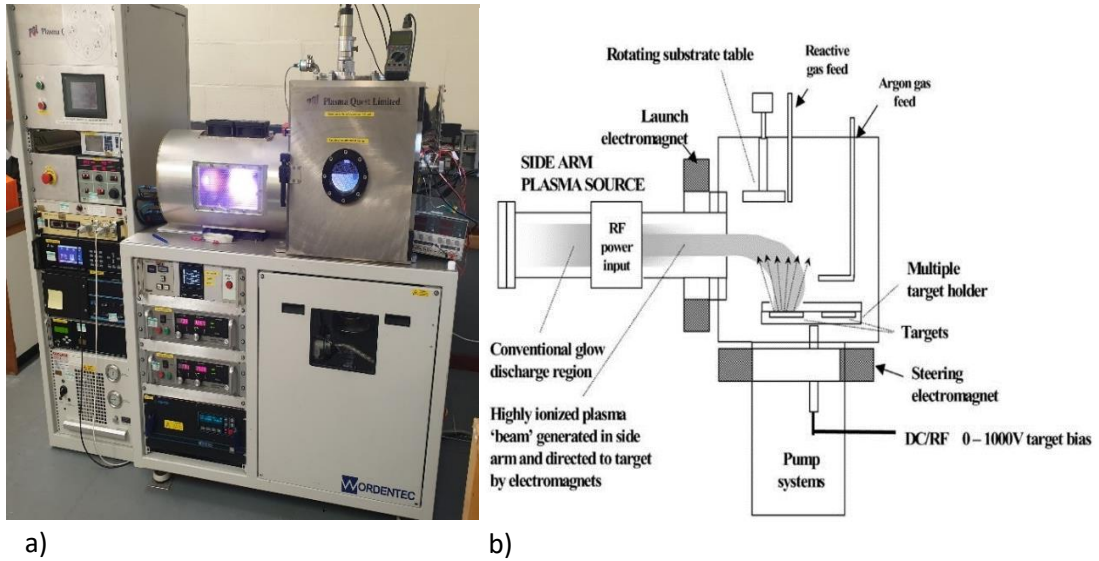
Figure 2.1a) A photo of HiTUS system and b) a schematic diagram of HiTUS [56].

The main advantage of using the HiTUS over other sputtering techniques is that it gives a user more control over different parameters such as grain size and deposition rate in comparison to other thin film deposition techniques such as Molecular Beam Epitaxy (MBE) and conventional magnetron sputtering. This control over sputtering parameters is particularly important for this study because of the controllability of compositions.

Plasma generation is not dependant on the target which results in no racetrack formation on the surface of the target that occurs with other conventional magnetron sputtering systems. This allows for approximately 90% [57] of the target to be sputtered and because there is near equal sputtering on the sample. It also gives the user the ability to change the stoichiometry of targets by placing pegs on top of the target.

The HiTUS allows a user to control sputtering parameters through DC bias voltage (0 – 1000 V), gas flow rate and the radio frequency (RF) power supply (0 – 3 kW).

A bias voltage must be applied to a target before sputtering can occur. In this system, a negative DC voltage of 0 – 1000 V can be applied onto a target. A minimum of -100 V is needed for the target current to become independent of the applied voltage. When the target becomes independent from the applied voltage, it remains constant as shown in *Figure 2.2*.
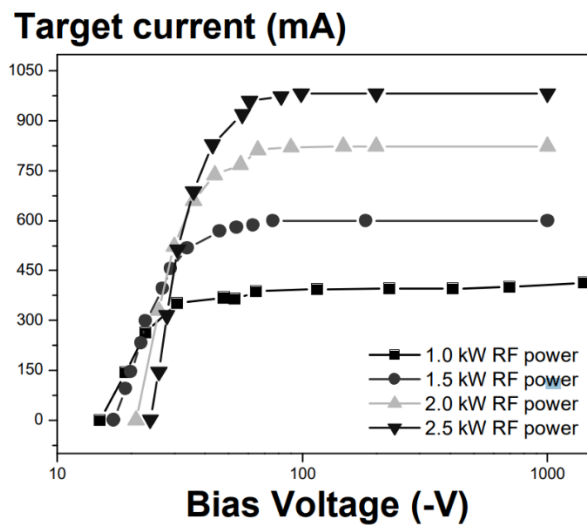
Figure 2.2: Graph of negative bias voltage vs target current for HiTUS [58].

Plasma is generated outside of the main chamber in the side arm of the deposition system. This allows the impact energy of the ions within the plasma to be controlled without affecting the high plasma density.

Argon (Ar) gas was used at base pressure 3×10^{-7} mbar. The flow rate of the Ar gas was controlled by an MKS® Mass Flow Controller (MFC). The MFC can set the gas flow rate to any value between 0 – 99 sccm. Varying the gas flow rate can change the Ar ion density which affects the pressure within the chamber.

The RF power supply is used to generate plasma. A 13.56 MHz rf electric field is coupled inductively with a coil within a quartz tube with a 25 kW, 3-turn rf antenna wrapped around the side arm of the HiTUS to produce plasma.

The Ar plasma flows into the main chamber by ambipolar diffusion. When the plasma is in the chamber, it can be directed towards the target by using the launch and steering electromagnets This creates magnetic fields of 50 Oe and 500 Oe respectively which confines the plasma into a beam along the magnetic flux lines of the electromagnets.

This beam of plasma does not have enough energy to sputter targets so a negative DC voltage of 1 – 1000 V is needed to accelerate the plasma beam in order to sputter the target.

The HiTUS allows for a maximum of six substrates to be sputtered during one deposition session without having to break the vacuum in the main chamber. Substrates are placed in substrate holders that are placed in a carousel with a shutter, meaning that samples are deposited one at a time. *Figure 2.3* shows the substrate holder used for this study.

Figure 2.3: A photo of a substrate holder used for this study.

Pre-cut silicon wafers that measure 10x10 mm^2 and 5x5 mm^2 were used for XRD and VSM measurement respectively. The sample holders used consisted of one 12x12 mm^2 square shaped hole and two square shaped 5x5 mm^2 holes. Sample holders with 12x12 mm^2 holes were used because they produced samples with the least amount of shadowing, maximising the volume of CoCrFeAl on a sample. Polyimide tape was used to secure the silicon wafers into place so that they did not become displaced during deposition.

The target carousel of the HiTUS can hold up to 8 targets, allowing for multilayer deposition during a single deposition session. The distance between the sample carousel and target carousel prevents re-sputtering and interactions between the generated plasma with the sample.

In order to fabricate high quality samples, it is important to clean both the silicon substrates and the target. The substrates are placed in a beaker with isopropanol in an ultrasonic bath for two minutes to remove dust and grease

from the surface of the substrate. Once the substrates are loaded in to the HiTUS, they are further cleaned for 10 seconds each by plasma. This is accomplished by turning off the steering magnet so that the plasma is released from its beam path and fills the chamber.

Targets are cleaned by sputtering the target with the shutter closed so that substrates do not get deposited on. The CoCrFeAl target was not used for a long period of time prior to this study so it was required to go through an aging process in order not to stress the target and cause it to crack. In this process, the target was sputtered at a low bias voltage and raised incrementally to the desired bias voltage. The initial sputtering voltage used was 100 V for two minutes, followed by increasing the bias voltage by 100 V increments until 900 V bias was reached. In subsequent deposition sessions, only 900 V is used to clean targets to remove any oxidation layers or particles on the surface of the target.

2.1.2 Annealing

A Carbolite CTF Wire-wound tube furnace was used for the post annealing treatment of CoCrFeAl thin films.

Figure 2.4: A photo of Carbolite, CTF Wire-wound tube furnace.

Samples were placed at the centre of a quartz tube so that there is an even distribution of heat. Parameters such as annealing temperature, annealing time

and step rates were adjustable through using the interface on the tube furnace. The furnace would anneal samples for the set duration and turn off automatically. Samples remained in the tube furnace until they cooled down to room temperature before being removed.

The tube furnace heating consists of a quartz tube. The quartz tube is open ended on one side which allows for the attachment of a vacuum pump. O-rings created a seal between the quartz tube and vacuum pump to prevent the leakage of gas. All samples were annealed in a vacuum with pressure ~3 x 10^{-8} mbar.

2.2   Structural Characterisation

2.2.1   X-Ray Diffraction

A Rigaku SmartLab X-ray diffractometer (XRD) was used in the study to investigate the structural characteristics of CoCrFeAl samples by using X-rays to identify a crystal structure of a sample. The principle of X-Ray diffraction can be expressed using Bragg's law:

$$n\lambda = 2d\sin\theta \tag{2.1}$$

where n is the order of diffraction, λ is the wavelength of the incident X-ray and θ is the angle of incidence and d is the lattice distance between two adjacent planes. CoCrFeAl has a cubic lattice formation which can be given by *equation 2.2*:

$$d = \sqrt{\frac{a^2}{h^2 + k^2 + l^2}} \tag{2.2}$$

where a is the lattice constant of a material and h, k and l are the Miller indices. Miller indices represent the orientation of an atomic plane.

Electrons are generated from a tungsten (W) cathode which bombard a rotating Copper (Cu) anode to generate X-ray which contain $Cu-K_{\alpha 1}$, $Cu-K_{\alpha 2}$ $Cu-K_{\beta}$, W-$L_{\alpha 1}$ and W-$L_{\alpha 2}$ wavelengths. A Germanium monochromator is used to filter $Cu-K_{\alpha 2}$ $Cu-K_{\beta}$, W-$L_{\alpha 1}$ and W-$L_{\alpha 2}$ wavelengths resulting in an X-ray beam that

consists of only $Cu-K_{\alpha 1}$ .This provides high resolution results due to the beam being easier to align by limiting beam divergence.
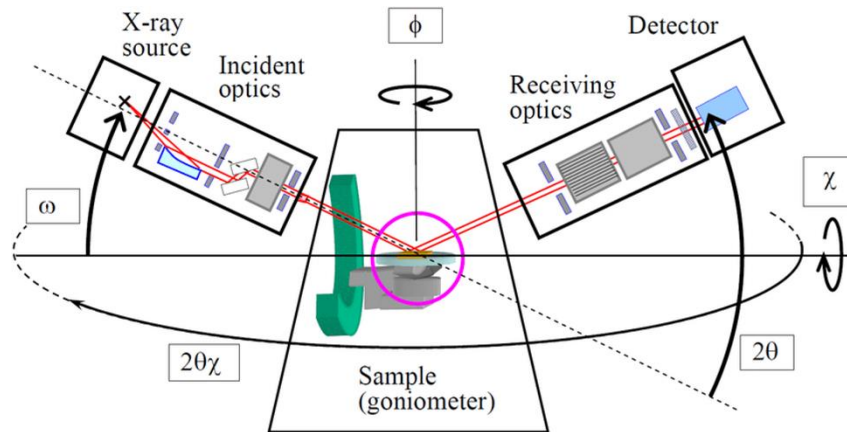
Figure 2.5: A schematic diagram of Rigaku Smartlab XRD system [59].

It is important to calibrate the XRD before performing a measurement by aligning the X-ray optics and sample in order to ensure precise and accurate measurements. Most of the alignment is managed by the Rigaku SmartLab software.

An optics alignment ensures that the incident X-ray beam is collimated and focused onto the sample so that the diffracted bream is accurately measured by the detector. This is done by aligning the three goniometer axes omega (ω), theta (θ) and 2theta (2θ). Alignment of the ω-axis ensures that the sample will be positioned at the correct height and distance relative to the X-ray incident beam by rotating the sample stage around the vertical axis; Alignment of the θ-axis ensures that the incident X-ray beam is centred on the sample and the reflected X-ray beam is accurately measured by the detector by moving the detector around the horizontal axis; Alignment of the 2θ-axis ensures the detector is at the appropriate angle relative to the sample by rotating both the detector and sample stage. The diffractometer software adjusts different instruments to optimise the alignment of various axes.

A sample alignment is needed in order to increase efficiency of measurements by finding the maximum signal by repeatedly adjusting the incident angle and sample stage height until a peak signal intensity is found. The process reduces the angular offset of the incident X-ray beam which increases the accuracy of measurements.

The two main XRD scans used for this study was θ-2θ general measurement and pole figure scan.

θ-2θ scan is used to check the crystal structure of the CoCrFeAl.
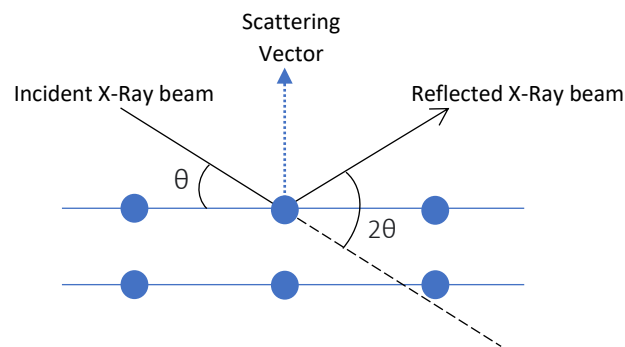
Figure 2.6: A schematic diagram of theta 2theta geometry for general measurements.

During a θ-2θ scan, the angle of the incident X-ray beam from the detector is half the angle of the reflected X-ray beam from the detector. This is done by constantly moving the X-ray source and detector so that the angle ratio is maintained. As a result, the scattering vector is always perpendicular to the sample which provides insight into the out of plane crystallographic information of CoCrFeAl samples.

2.3   Chemical Characterisation

2.3.1   Scanning Electron Microscope

A JEOL JSM-7800F Prime scanning electron microscope (SEM) fitted with dual Oxford Instrument energy dispersive X-ray (EDX) detector was used in the study to measure the stoichiometry of CoCrFeAl samples.
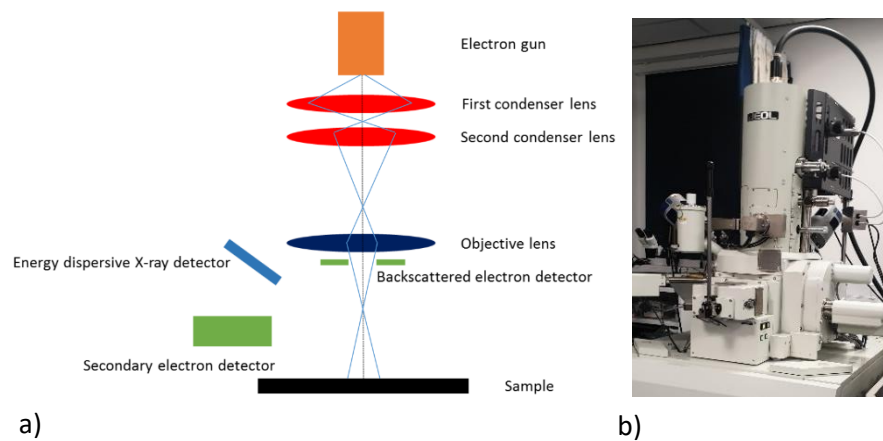
Figure 2.7: a) schematic diagram of SEM [60] and b) picture of JEOL JSM-7800F.

SEM-EDX is a powerful technique for analysing the composition of a sample. A SEM consists of three key components; an electron gun; magnification lenses and detectors. The electron gun within this system is an in-lens Schottky field emission gun [61] which generates an electron beam. An anode accelerates the beam which is then collimated and focused by electromagnetic lenses on the sample. The detector converts the X-rays into electrical signals which are processed by a computer within the control.
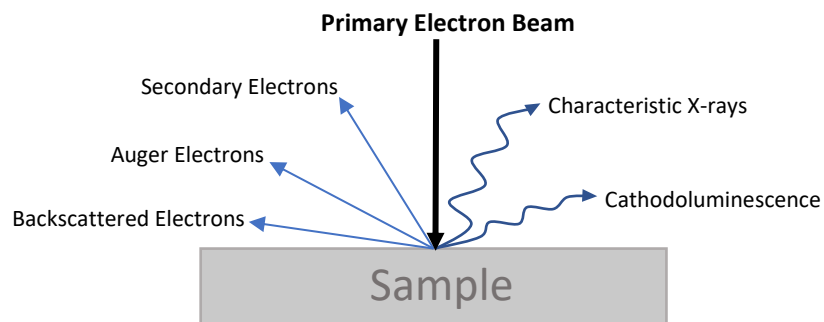
Figure 2.8: Schematic diagram of electron beam interactions.

Figure 2.8 shows the variety of phenomena that occur when the electron bean interacts with a sample. These phenomena can be divided into two types of interactions; elastic and inelastic scattering.

Elastic scattering interactions produces backscattered electrons. Some electrons from the electron beam may be scattered back out of the specimen due to interactions with an atom's nuclei. These are called backscattered

electrons. The backscattered electron signal is related to the atomic number of the material.

Inelastic scattering interactions produces secondary electrons. When the electron beam hits the surface of the specimen, some electrons collide and interact with an atom within the sample and transfers energy to the atom which can cause ionisation or excitation.

Another form of inelastic interaction is the production of Auger electrons. Auger electrons are low-energy electrons that are emitted after ionisation caused by an incident electron beam transferring energy to an electron residing in the inner shell of an atom and subsequently ejecting it. When an electron from a higher energy level drops down to fill the vacancy left by the ejected electron an Auger electron is emitted. The energy of the Auger electrons is specific to the elemental composition of a sample.

A phenomenon referred to as cathodoluminescence occurs when the specimen emits light after being excited by the electron beam. Cathodoluminescence is a result of inelastic scattering. In this process, the electron beam transfers energy to the sample which excites electrons within the material. When the excited electrons return to their ground state, it emits photons that have a corresponding energy difference to the energy difference between the ground and excited states.

Characteristic X-rays is similar to cathodoluminescence in that they are both photons generated through inelastic scattering. However, a key difference is that characteristics X-rays are generated by ionisation rather than excitation. Spectra of X-rays is generated and can be detected using EDX, which provide information about the elemental composition of a sample.

Due to the experimental nature EDX technique, the chemical composition analysis has an error of approximately 10% as a result of the large interaction volume and the inhomogeneous deposition of the CoCrFeAl samples used in this study.

2.4   Magnetic Characterisation

2.4.1   Vibrating Sample Magnetometer

A Vibrating Sample Magnetometer (VSM) was used in this project in order to measure the magnetic characteristics of CoCrFeAl samples. *Figure 2.9* shows a schematic diagram of a VSM.

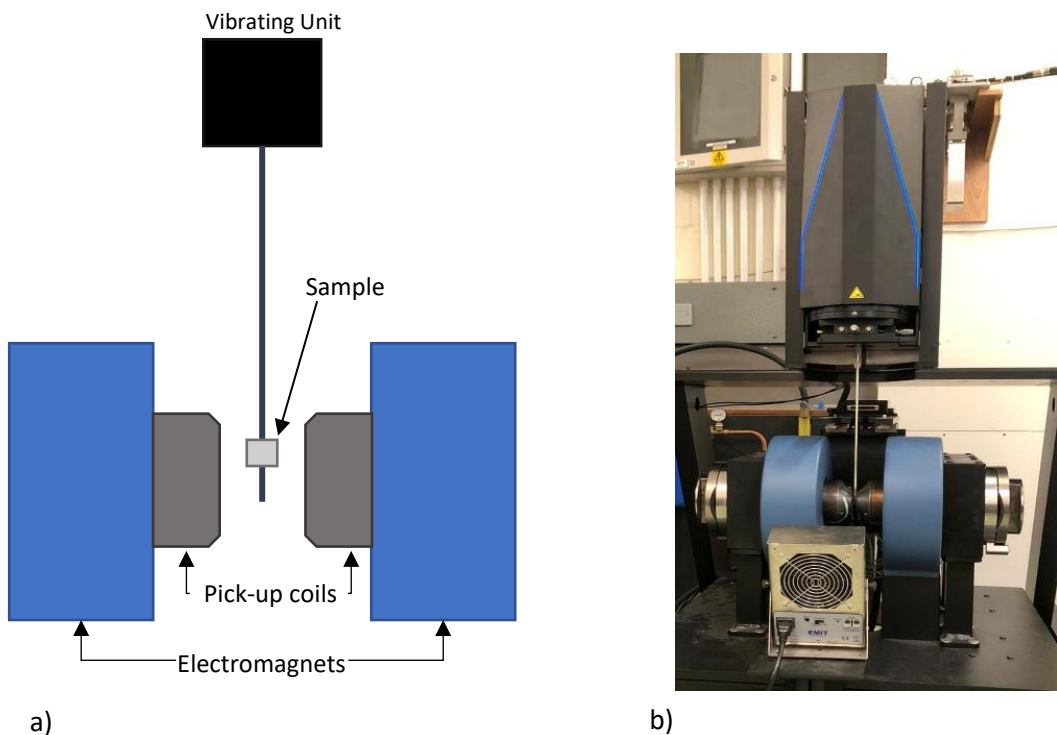Figure 2.9: a) schematic image of VSM and b) photo of Lakeshore Series 8600 VSM.

Faraday's law of induction is used to measure the magnetic properties of a sample in an open circuit by detecting voltage induced by the change in magnetic flux. This process is called electromagnetic induction and can be represented by *equation 2.3* [62]:

$$\varepsilon = -N \, \frac{\partial \emptyset_B}{\partial t} \qquad (2.3)$$

where ε represents the induced voltage, $\emptyset_B$ represents the magnetic flux generated by the sample and N is the number of turns in the coil.

The sample is vibrated in between the two coils in order to induce a change of flux. The total magnetic flux penetrating a sample is determined by the applied magnetic field (H), the magnetisation (M) of the sample and the cross-sectional area of the coils (A_c). The relationship of these variables is shown in *equation 2.4*:

$$\emptyset_B = (H + M) \cdot A_c \tag{2.4}$$

An electromotive force (e.m.f.) is produced when is a sample is vibrating which can be calculated using Faraday's law and can be expressed as seen in *equation 2.5* by combing *equations 2.3* and *2.4*:

$$\int \varepsilon \cdot \partial t = -NA_c \cdot M \tag{2.5}$$

Given that H does not vary with time and remains constant, the induced e.m.f voltage is only directly proportional to the sample magnetisation.

This VSM model has a high sensitivity of 1.5×10^{-8} emu at room temperature with a maximum field of 23.7 kOe.

Magnetisation curves will be compared in this study, so it is important to regularly calibrate M before use to ensure accurate measurements to make comparisons more accurate in analysis. For thin film measurements, palladium (Pd) foil is used for calibration because it is a Pauli paramagnet with linear magnetic susceptibility. Palladium is the most ideal material to use because its magnetisation always remains constant in an applied field, magnetic susceptibility remains at 5.26×10^{-6} cm^3/g [63] regardless of change in temperature, and it is highly resistant to corrosion.

VSM generates magnetisation curves, also known as hysteresis loops, that provide information about the magnetic properties of a sample such as its coercivity, saturation magnetisation.

2.5 Electrical Characterisation

2.5.1 Four Point Probe Method

A four-point probe station (HiSOL, HMP-4000 SMS) was used to measure the electronic properties of CoCrFeAl samples.
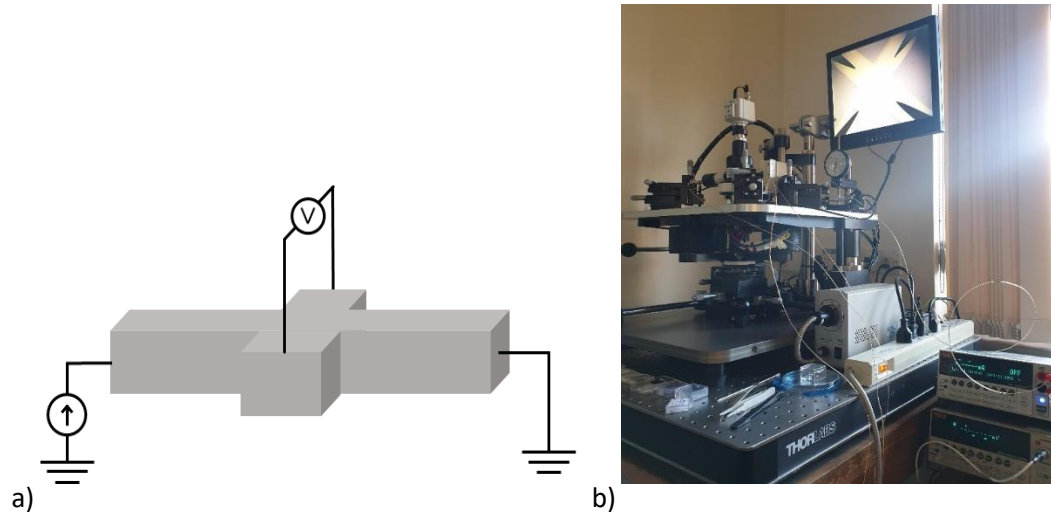
Figure 2.10: a) schematic diagram of four point probe geometry and b) picture of four point probes on a sample.

The four-point terminal method, also known as Kelvin measurement, was used to measure the voltage drop across the inner terminals when a DC current was applied across the two outer terminals. This method was used to measure the spin Hall effect of a material by applying a magnetic field is applied perpendicular to the direction of the current. Configuring the measurement this way provides a highly accurate measurement of resistance because the contact resistance of the probes is negligible. This is due to voltmeters having a high impedance, which causes current to only flow between the outer terminals. Therefore, any voltage measured by the probe is due to the spin Hall voltage generated in a sample.

3. Results and Discussion

The main aim of this work is to investigate the spin Hall effect of the CoCrFeAl Heusler alloy. All thin films in this study were deposited by the HiTUS. Thin films were grown with a thickness of 20 nm on silicon substrates at bias voltage 900 V. The deposition rate of the CoCrFeAl thin films was 0.06 nm/s. Silicon substrate was used due to its compatibility with the industry standard for fabricating devices.

3.1 Optimisation of CoCrFeAl

It was important to investigate the chemical stoichiometry of the sample in the target in order to check if there were any element deficiencies and to confirm 1:1:1:1 as a quaternary Heusler alloy as discussed in *Section 1.3* since the structure of a Heusler alloy can have a strong impact on the magnetic and electronic properties of a Heusler alloy.

SEM-EDX was used to analyse the chemical composition of both the target and the first three initial samples. An electron beam of 15 eV was used because too low an energy beam would not be sufficient enough to penetrate the target or the samples and an electron beam with too much energy would destroy the samples. The SEM-EDX analysis was conducted by Dr David Lloyd for the undoped samples, and Fayzah Talbi for doped samples.

Three samples were initially deposited to investigate the average chemical properties of CoCrFeAl with undoped growth conditions.

Element	Target	Sample 1	Sample 2	Sample 3
Co	28.9	2.6	2.8	2.8
Cr	22.6	1.4	1.5	1.5
Fe	26.6	2.1	2.2	2.2
Al	21.9	1.0	1.1	1.1

Table 1: shows the SEM-EDX results of the atomic weight of Co, Cr, Fe and Al in the target and three samples.
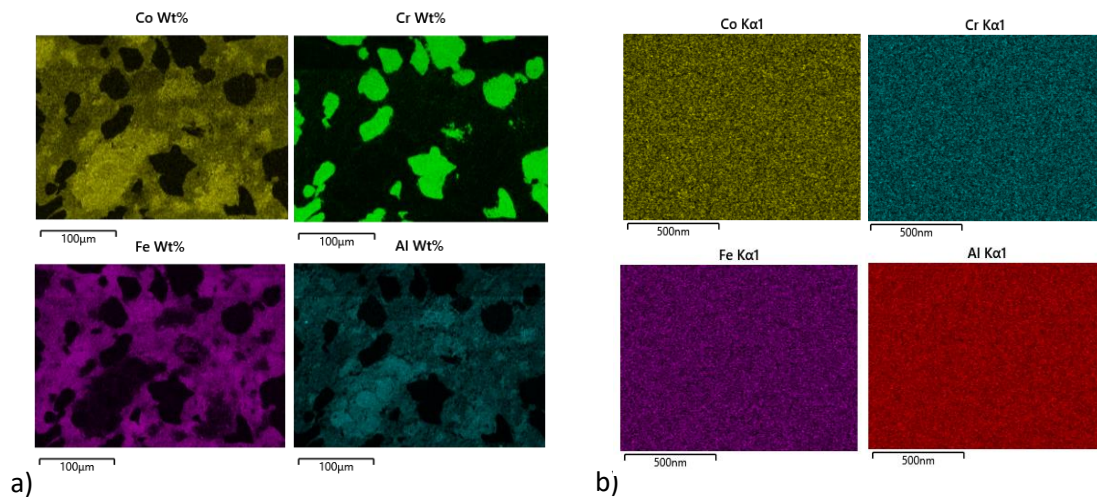
Figure 3.1: Shows the EDX mapping of constituent elements of CoCrFeAl for the a) target and b) a deposited thin film.

EDX-Mapping showed that the elements within the CoCrFeAl sputtering target were not evenly distributed, especially for Cr where there were distinct islands of Cr observed, as shown in *Figure 3.1a*. Fortunately, this did not directly lead to uneven distribution of elements on the deposited samples as seen in *Figure 3.1b.*

When normalised, the target has a ratio of 1: 0.78: 0.92: 0.76 and the mean of three samples has a ratio of 1: 0.55: 0.81: 0.40 of Co, Cr Fe and Al respectively. From the analysis of the film and target, it is apparent that the deficiency of Cr and Al mostly stem from the deficiency of the respective elements in the target. As a result, it was important to optimise the deposition to provide the ideal stoichiometry of 1:1:1:1. Despite Cr and Al having a slight difference of values in terms of the atomic weight and deficiency in the target, it is evident that these samples possessed a higher deficiency of aluminium compared to the target. This could be due to aluminium having a lighter atomic weight than Cr, Fe and Fe (26.980 g/mol to 51.996 g/mol, 58.933 g/mol and 55.847 g/mol respectively) which makes Al atoms more likely to be deflected away from the substrates during deposition by the Argon gas.

In order to achieve the stoichiometry of the samples, the target was machined by Jason Flatt, senior technician of the mechanical workshop at the University of York. *Figure 3.2* shows the machined target. Al and Cr pegs were also acquired and cut into pegs so that they could fit into the drilled holes of the target. Al and Cr pegs measured 3 mm and 2 mm in diameter respectively and were of lengths 2 mm. 2 mm rod length was chosen as

Figure 3.2: A picture of drilled CoCrFeAl target. Cr Peg held by tweezers.

it was approximately half the height of the target. This was done to avoid compromising the structural integrity of the target in order to reduce the likelihood of cracks forming during deposition. When the diameter of the pegs was known, corresponding hole diameters of 3 mm and 2 mm were drilled 2mm deep so that the pegs were near flush against the target surface in order to minimise the risk of charging and voltage arcing during deposition.

Growth Conditions	Compositions
CoCrFeAl	1 : 0.55 : 0.92 : 0.40
CoCrFeAl with 1 Al peg	1 : 0.73 : 0.89 : 0.84
CoCrFeAl with 1 Cr peg	1 : 0.82 : 0.91 : 0.78
CoCrFeAl with 1 Al and 1 Cr pegs	1 : 0.77 : 0.91 : 0.83
CoCrFeAl with 2 Al and 1 Cr pegs	1 : 0.74 : 0.91 : 0.81
CoCrFeAl with 1 Al and 2 Cr pegs	1 : 0.77 : 0.92 : 0.86
CoCrFeAl with 2 Al and 2 Cr pegs	1 : 0.78 : 0.94 : 0.85

Table 2: shows the different combinations of Al and Cr pegs used to improve the stoichiometry of the samples.

3.1.1 XRD Data of initial sample

XRD analysis of the initial as deposited samples were performed to see whether the sample would crystallise as deposited at room temperature without post-annealing. By comparing the XRD plot with theoretically calculated values and previous experimental work by Kharel *et al.* [53], it was possible to determine if the samples were crystallised as a peak would be present near the same degree presented in their paper or near the theoretical values. *Table 3* shows the theoretical peak angles calculated using Bragg's law and the approximate XRD peak angles identified in Kharel's experimental work.

Theoretical Degree Angle (°)	*Approximate Degree Angle (°)*	*Reflection Peak*
27	26.5 ± 2°	(111)
31	31 ± 2°	(200)
45	44 ± 2°	(220)
55	55 ± 2°	(222)
74	70 ± 2°	(420)

Table 3: Theoretical and experimental reflection peaks in arc-melted CoCrFeAl, adapted from the results obtained experimentally by Kharel *et al.* [53].

For an ordered $L2_1$ phase, reflection peaks (220), (200) and (111) would typically be present in an XRD theta-2theta scan. For $B2$ type disorder, peaks (200) would be expected and for $A2$-type disorder, a principle reflection peak (220) and another peak possibly at (420) depending on the severity of the disorder within the structure.
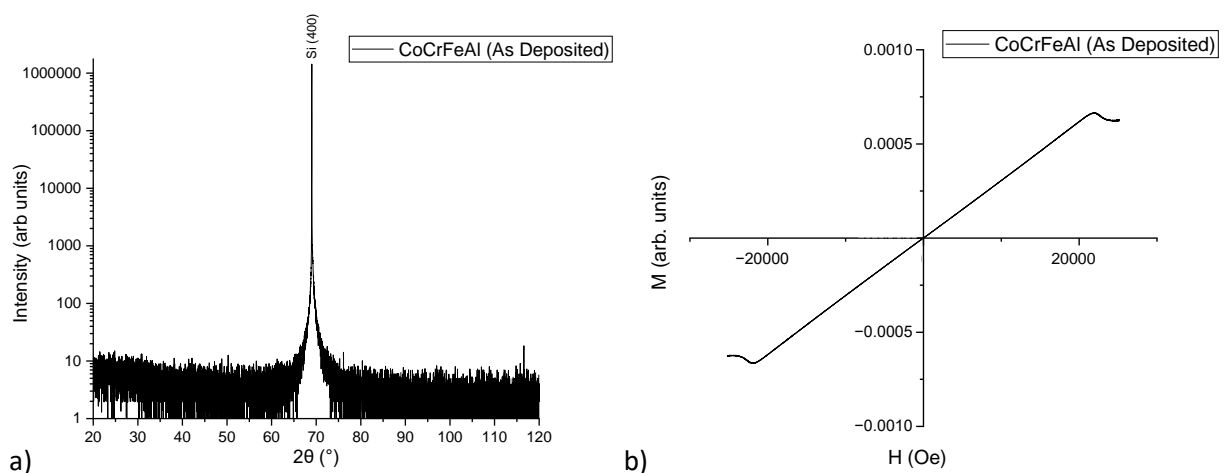

Figure 3.3: a) XRD scans for 20 nm CoCrFeAl sample deposited at room temperature b) VSM scan for 20 nm CoCrFeAl sample deposited at room temperature

Figure 3.3a shows the XRD scan of the initial CoCrFeAl film in its as deposited state. No peaks are identified but the background intensity of the XRD signal increases with decreasing the diffraction angle, which indicate the presence of amorphous phase. A VSM measurement was conducted to determine magnetic properties of the as-deposited samples, which would also give further information about crystal structure. If a magnetic hysteresis loop is obtained, it would indicate that any peaks were too subtle be observed from the XRD scan. The kinks at the positive and negative saturation are due to the paramagnetic contributions of the components used to hold the sample in place on the sample rod such as vacuum grease and Polytetrafluoroethylene (PTFE) tape.

 The VSM measurement only showed linear behaviour, which indicated that the sample was paramagnetic. Due to the lack of reflection peaks and no indication of magnetic behaviour the CoCrFeAl samples were assumed to be amorphous.

In order to improve the crystallinity, CoCrFeAl samples were annealed *ex-situ* at elevating temperatures between 300 and 500°C for 2 hours. An annealing temperature of 600°C was attempted to investigate if 600°C would provide better crystal structure or cause diffusion of Cr and Al from the lattice. However, this resulted in the cracking of the quartz tube used in for the tube furnace, as seen in Figure 3.4 so higher temperatures were not attempted again.

Figure 3.4: A photo of the cracked quartz tube for the tube furnace.

The XRD theta-2theta scan, shown in *Figure 3.5*, shows that when samples are annealed at 300°C, the samples show no reflective peak. VSM data confirms that the sample was amorphous, possibly paramagnetic as similar to the as-deposited films. At 400°C, a very subtle peak was observed around 45° (44.63°) as shown in *Figure 3.5e*. This gave a lattice constant of 5.7433 Å.

Further investigation of the scan showed that no other peaks ((200), (111) or (420)) were present. By comparing the peak position with theoretical predictions and previous experimental results, it is clear that this was a principle (220) peak [53].

Thus, the ordering temperature for CoCrFeAl deposited by the HiTUS lies between 300°C and 400°C. The (220) reflection peak confirms that the sample had crystallised with at least *A*2-type ordering.

Samples post-annealed at 500°C showed nearly identical intensity of the (220) peak as that obtained by annealing at 400°C; this can be seen in *Figure 3.4e*. Given that the only peak observed is a CoCrFeAl peak, it indicated that *ex-situ* annealing temperatures up to 500°C are not high enough to cause segregation of the constituent elements from the lattice structure in undoped CoCrFeAl as no Co, Cr, Fe and Al peaks were observed.
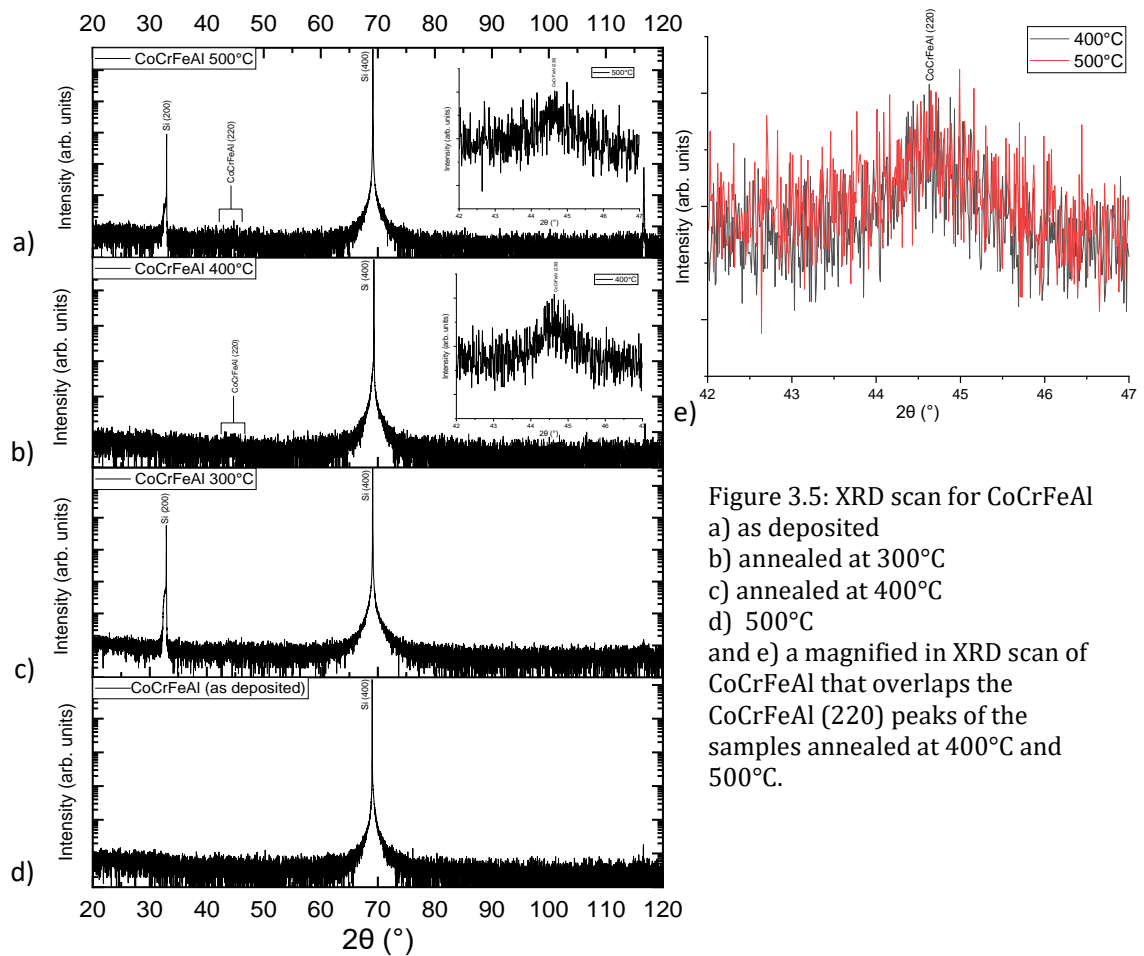

Figure 3.5: XRD scan for CoCrFeAl
a) as deposited
b) annealed at 300°C
c) annealed at 400°C
d) 500°C
and e) a magnified in XRD scan of CoCrFeAl that overlaps the CoCrFeAl (220) peaks of the samples annealed at 400°C and 500°C.

3.1.2 XRD of doped samples

Figure 3.6 shows the XRD theta-2theta scans of doped samples (1 Al peg, 1 Cr peg, 1 Al and 1 Cr pegs) at different annealing temperatures. It indicates that although doping improved the stoichiometry, it had very little impact on the ordering temperature as it follows the trend of the initial undoped samples. For $CoCr_{0.73}Fe_{0.89}Al_{0.84}$ (1 Al peg doping), the principle (220) peak is observed at 44.61° and 44.67° for annealing temperatures 400°C and 500°C respectively. For $CoCr_{0.83}Fe_{0.91}Al_{0.78}$,(1 Cr peg doping) the principle peak is observed at 44.52° and 44.63° respectively and likewise for $CoCr_{0.77}Fe_{0.90}Al_{0.83}$ (1 Al and 1 Cr pegs), principal (220) peaks are observed at 44.59° and 44.52° respectively. No other reflective peaks were observed in the scan which indicates that all CoCrFeAl samples, regardless of annealing, remained in the *A*2-type phase. The broadness of the peak also suggests weak crystallinity. Given the low intensity of the peaks, all rocking curve measurements gave inconclusive results therefore it was difficult to investigate the crystal structure further by in-plane XRD analysis. All samples are assumed to have a typical experimental error of ±10%.

The observed peaks were used to calculate the d-spacing using the following *equation 3.1*:

$$d_{hkl} = \frac{\lambda}{2\sin\theta} \qquad\qquad (3.1)$$

The *d*-spacing was then used to determine the lattice parameter (a) of each sample using *equation 3.2*:

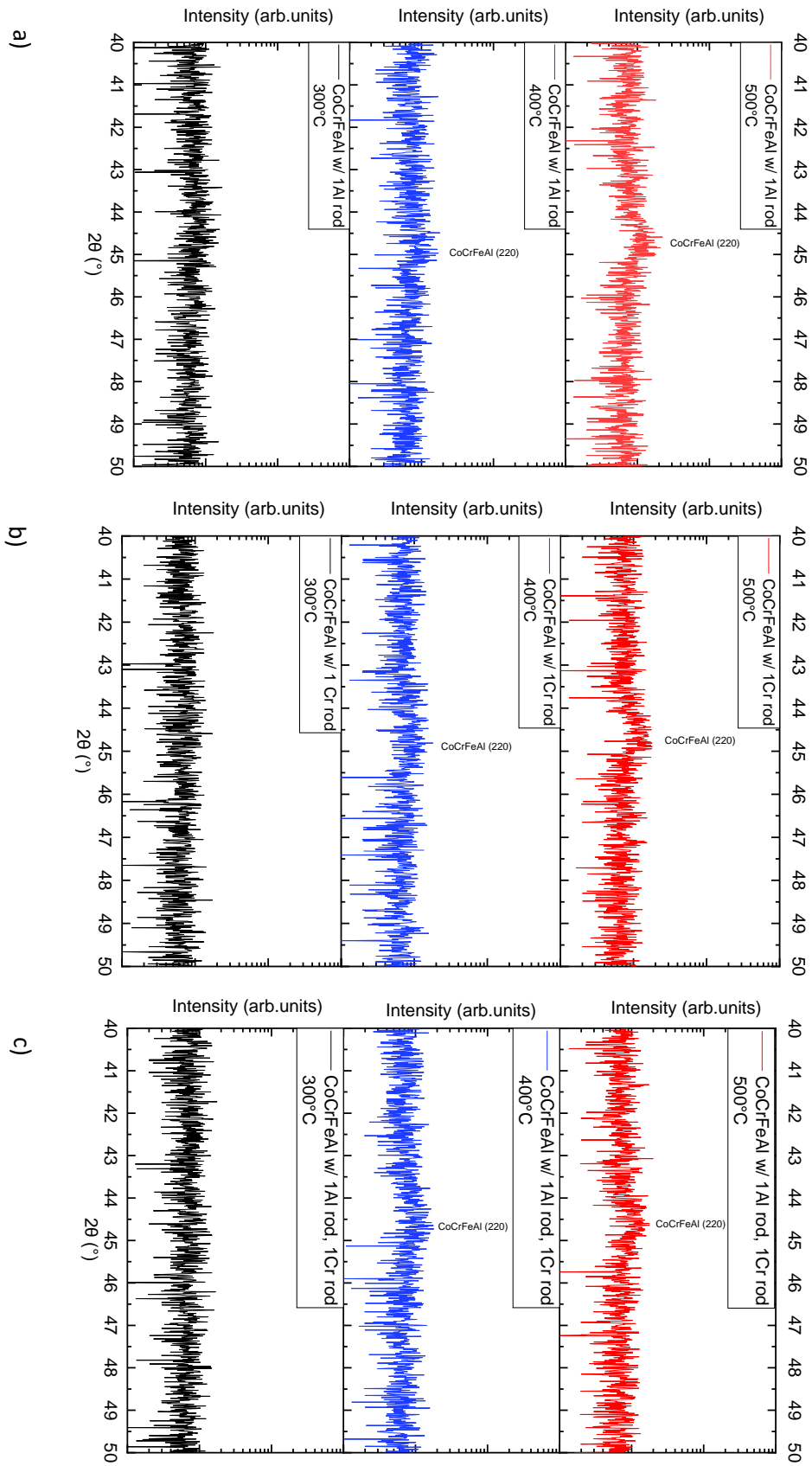$$a = d_{hkl}\sqrt{(h^2 + k^2 + l^2)} \qquad\qquad (3.2)$$

Figure 3.6: a) XRD theta-2theta plot of CoCrFeAl sample doped with 1 Al peg, b) CoCrFeAl sample doped with 1 Cr peg c) CoCrFeAl sample doped with 1 Al and 1 Cr pegs.

Sample	Bragg's angle (°)	d-spacing (Å)	Lattice constant (Å)
undoped	44.6370	2.0284	5.7372
$CoCr_{0.73}Fe_{0.89}Al_{0.84}$ annealed at 400°C	44.6166	2.0293	5.7397
$CoCr_{0.73}Fe_{0.89}Al_{0.84}$ annealed at 500°C	44.6661	2.0272	5.7337
$CoCr_{0.83}Fe_{0.91}Al_{0.78}$ annealed at 400°C	44.5219	2.0334	5.7513
$CoCr_{0.83}Fe_{0.91}Al_{0.78}$ annealed at 500°C	44.6312	2.0287	5.7379
$CoCr_{0.77}Fe_{0.90}Al_{0.83}$ annealed at 400°C	44.5919	2.0304	5.7427
$CoCr_{0.77}Fe_{0.90}Al_{0.83}$ annealed at 500°C	44.5235	2.0333	5.7511

Table 4: A comparative table showing the observed Bragg's angle, d-spacing and lattice constant of samples doped with Al and Cr pegs post annealing.

The theoretical value of CoCrFeAl is 5.7 Å [48]. This supports the experimental values derived from the XRD measurements as they lie within ± 1% of the theoretical value. A Gaussian fit was used to generate a curve of best fit to obtain the Bragg's angle from the data. Given how little the lattice constant deviates from the theoretically predicted value, it is assumed that the variation is due to compositional changes.

Another attempt was made to further improve the stoichiometry of the samples by increasing the number of pegs used; 2 Al and 1 Cr peg, 1 Al and 2 Cr pegs, and 2 Al and 2 Cr pegs. This yielded the chemical composition of 1: 0.74: 0.91: 0.81, 1: 0.77: 0.92: 0.86 and 1: 0.78: 0.94: 0.85 respectively. The SEM-EDX analysis showed that the increase of pegs improved the stoichiometry of the samples, however further XRD analysis was needed to determine if one of the above mentioned composition was the optimal composition.

Figure 3.6 shows the XRD theta-2theta plot of the 2 peg doped samples. Initially, it appears that these samples follow the same trend as seen in *Figure 3.5a – c*. However, subsequent XRD theta-2theta scans show that the deposited 2 Al and 1 Cr peg sample produced poor XRD scans with low intensity. This made it impossible to analyse the crystal structure through XRD analysis. This may

indicate the additional changes in the composition may induce some phase segregation in the films, degrading the crystallinity.
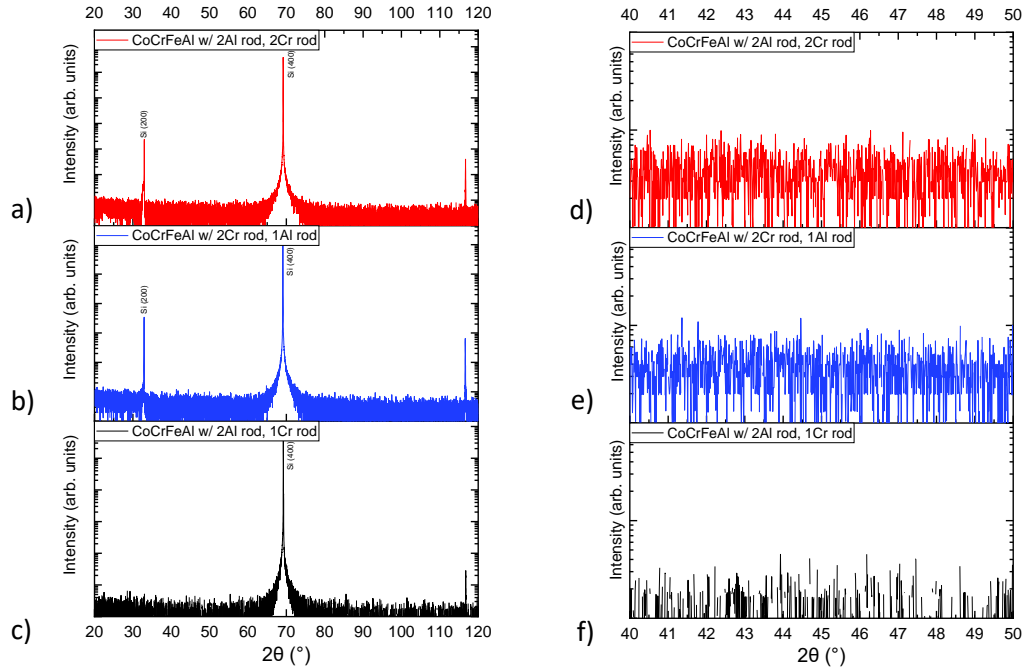

Figure 3.7: a-c) shows a full theta-2theta scan of CoCrFeAl samples doped with 2 Al and 1 Cr pegs, 1 Al and 2 Cr pegs, and 2 Al and 2 Cr pegs. d-f) shows a magnified in theta-2theta scan at the expected range for the CoCrFeAl principle (220) peak.

Whilst there was no colour change or change in transparency of the sample surface and samples were stored in a vacuum sealed dessicator when not in use, oxidation of the sample was considered as a possible answer. If oxidation was the case, it may be due to aluminium because it first occurred with the sample with 2 Al and 1 Cr pegs. Aluminium is an element that oxidises easily so it is possible that the aluminium segregated from the lattice struture allowing for oxidation to occur. The possibility of oxidisation was further supported with subsequent XRD scans of the annealed samples which produced plots similar to *Figure 3.7f* for all annealed samples regardless of doping amount where at one element had two pegs.

One of the optimisation aims is to improve the stoichiometry of the deposited CoCrFeAl thin film, therefore doped samples were investigated further.

3.1.3 VSM data analysis of doped samples

Given how small the difference between the XRD scans of the doped samples are seen in *Figure 3.6*, magnetic characterisation was conducted to investigate the magnetic properties of CoCrFeAl and see if there are any noticeable differences between samples that may have been missed by the XRD due small volume, which may only induce low counts of the peaks.

The doped samples followed the trend of exhibiting paramagnetic behaviour in the as deposited state and when annealed at 300°C for 2 hours which confirmed the samples to be amorphous. The sample exhibited ferromagnetic behaviour after ex-situ annealing at temperature of 400°C and 500°C for 2 hours. *Figure 3.7* shows the magnetic response for $CoCr_{0.73}Fe_{0.89}Al_{0.84}$ (1 Al peg doping), $CoCr_{0.82}Fe_{0.91}Al_{0.78}$, (1 Cr peg doping) and $CoCr_{0.77}Fe_{0.90}Al_{0.83}$ (1 Al and 1 Cr pegs doping).
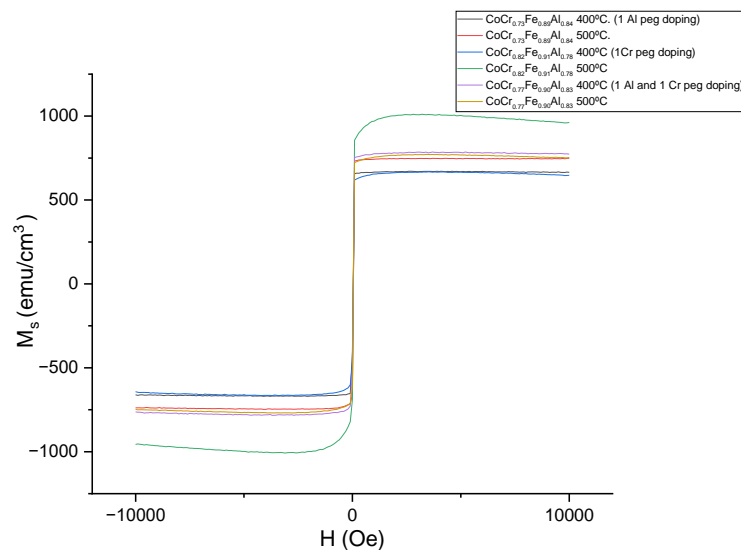
Figure 3.8: hysteresis loops of 1 peg doped samples.

Sample Composition	Saturation Magnetisation (emu/cm^3)	Coercivity (Oe)	Squareness
$CoCr_{0.73}Fe_{0.89}Al_{0.84}$ annealed at 400°C	670	37.8	0.66
$CoCr_{0.73}Fe_{0.89}Al_{0.84}$ annealed at 500°C	838	48.7	0.79
$CoCr_{0.83}Fe_{0.91}Al_{0.78}$ annealed at 400°C	783	43.2	0.61
$CoCr_{0.83}Fe_{0.91}Al_{0.78}$ annealed at 500°C	748	49.9	0.92
$CoCr_{0.77}Fe_{0.90}Al_{0.83}$ annealed at 400°C	987	42.1	0.51
$CoCr_{0.77}Fe_{0.90}Al_{0.83}$ annealed at 500°C	770	47.0	0.80

Table 5: A table showing the chemical composition of CoCrFeAl samples with corresponding saturation magnetisation, coercivity and squareness.

The estimated saturation magnetisation of the samples shown in *Figure 3.8* is presented in *Table 5*. The value that is theoretically predicted for CoCrFeAl is approximately 784 emu/cm^3, derived from the generalised Slater-Pauling curve calculated by Özdoğan *et al.* [48]. It is found that the magnetisation saturation of the samples doped with only Cr pegs are above 100% the theoretical value. This could be due to Cr alloying with another element or phase segregation which may lead to the formation of a different crystal type which would show different magnetic properties.

Figure 3.8 shows the samples doped with Al peg exhibited an increase in magnetic saturation after annealing, which resulted in an increase of magnetisation. This is supported by the improvement of the (220) principle peak as seen in *Figure 3.5a*.

Samples doped with both Al and Cr pegs at annealing temperature 400°C and 500°C are approximately 98% and 100% of the theoretical saturation magnetisation value, with no significant change observed with the XRD scan. This suggests that when the CoCrFeAl target used in this sample is doped with 1 Al and 1 Cr peg, the resultant sample is less susceptible to phase segregation compared to samples deposited with only the Cr pegs.

All 1 peg doped samples show coercivity below 50 Oe. The low values of coercivities indicates that CoCrFeAl is magnetically soft which is an ideal property for spintronic devices as it allows for more efficient magnetic reversal. An increase in coercivity is seen in the hysteresis loops in *Figure 3.7* as annealing temperature increases. This could be attributed to an increase in grain size. It is also observed that the squareness ratio increases with anneal temperature, this could be due a decrease in texture quality.
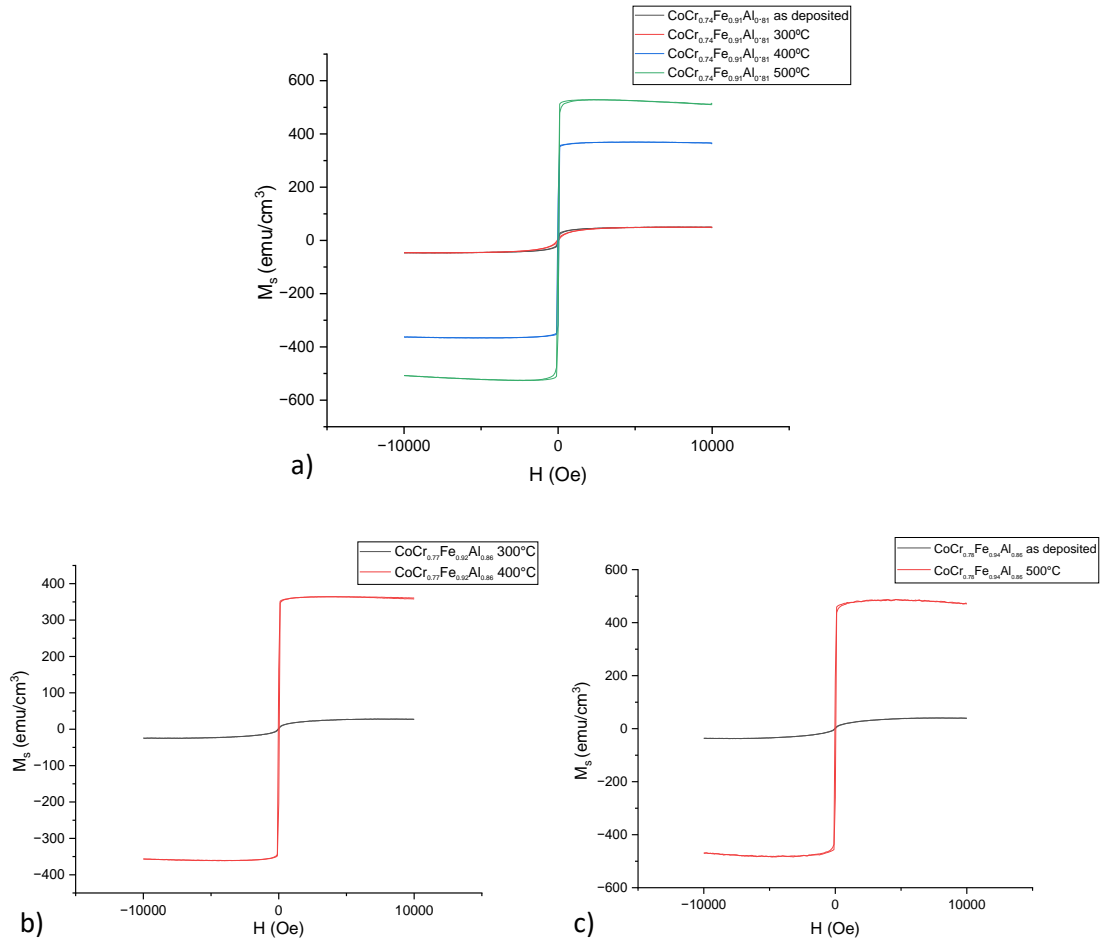
Figure 3.9: hysteresis loops of 2 peg doped samples a) 2 Al and 1 Cr pegs, b) 1 Al and 2 Cr pegs, and c) 2 Al and 2 Cr pegs.

Sample Composition	Saturation Magnetisation (emu/cm^3)	Coercivity (Oe)	Squareness
CoCr$_{0.74}$Fe$_{0.91}$Al$_{0.81}$ as deposited	49	23.9	0.02
CoCr$_{0.74}$Fe$_{0.91}$Al$_{0.81}$ annealed at 300°C	49	28.0	0.12
CoCr$_{0.74}$Fe$_{0.91}$Al$_{0.81}$ annealed at 400°C	369	48.1	0.11
CoCr$_{0.74}$Fe$_{0.91}$Al$_{0.81}$ annealed at 500°C	524	41.4	0.30
CoCr$_{0.77}$Fe$_{0.92}$Al$_{0.86}$ annealed at 300°C	27	-9.4	0.11
CoCr$_{0.77}$Fe$_{0.92}$Al$_{0.86}$ annealed at 400°C	364	37.3	0.36
CoCr$_{0.78}$Fe$_{0.94}$Al $_{0.86}$ as deposited	38	1.8	0.07
CoCr$_{0.78}$Fe$_{0.94}$Al $_{0.86}$ annealed at 500°C	485	48.4	0.37

Table 5: A table showing the chemical composition of 2 pegs doped CoCrFeAl samples with corresponding saturation magnetisation, coercivity and squareness.

Although XRD analysis was not possible with 2 peg doped samples, VSM measurements give an insight into the magnetism of these doped samples.

Samples doped with 2 Al and 1 Cr pegs have 6%, 6%, 47% and 68% of the theoretical saturation magnetisation value for the as deposited state and annealing temperature of 300°C, 400°C and 500°C respectively. Hysteresis loop in the as deposited state and at annealing temperature 300°C provided a different result compared to undoped and 1 peg doped samples at the same temperature. Very small saturation magnetisation, indicated by the value being a magnitude lower than the theoretical value, indicated that $CoCr_{0.74}Fe_{0.91}Al_{0.81}$ may be polycrystalline with relatively smaller grain sizes in comparison to the other sample compositions in its as deposited state. Given that the magnetisation value at 300°C and the as deposited sample are the same, it is possible that the magnetisation rotation dominates the magnetisation process until it reaches its ordering temperature. CoCrFeAl samples doped with 2 Al and 1 Cr pegs remained a soft magnet but have a lower squareness ratio compared to 1 peg doped samples.

Samples doped with 2 Cr pegs and either 1 or 2 Al peg(s) displayed a similar trend to samples doped with 2 Al and 1 Cr pegs in terms of improved magnetisation once ordering temperature is reached.

Increased doping may contribute to phase segregation which leads to a change in hysteresis shape as a of product of the change in the saturation magnetisation.

3.1.4 Optimum Conditions

The growth conditions with 1 Al and 1 Cr pegs with *ex-situ* annealing temperature of 400°C was chosen as the optimal growth conditions.

When comparing magnetisation, this growth condition provided the most favourable magnetisation saturation at 783 emu/cm^3 which is nearly 100% of the theoretical magnetisation saturation value.

For industrial fabrication, a low temperature is preferred in order not to damage temperature sensitive components of devices. Given that the difference of magnetisation and crystallinity is not substantial between the 400 and 500°C post annealing temperatures, 400°C is the more appropriate choice.

Finally, when the ~10% error from EDX is considered, doping with 1 Al and 1 Cr peg provides the closest to 1:1:1:1 stoichiometry by increasing the Al and Cr content by ~100% and 20% with respect to the undoped samples whilst also proving to be the most stable composition when compared to two peg doped samples combinations which appear to be more susceptible to phase segregation.

3.2   Spin Hall Experiment

The spin Hall effect was measured using the method described in *Section 2.5*. The CoCrFeAl Hall bar measured approximately 10 mm probe separation vertically and horizontally across, with the terminals having a width of 1 mm. The current probes were placed on the horizontal terminals with a distance of approximately 3.33 mm and the voltmeter probes were placed on the vertical terminals with a distance of approximately 1.51 mm between the two probes. A magnetic field of 2 kOe was applied in the same orientation as the current flow. A current of 1 mA was used.

For a spin gapless semiconductor, it is expected for there to be a large spin Hall effect to be present because the unique band structure would allow for the spin polarised electrons to accumulate on opposite sides of a sample depending on their spins with minimal energy required [64].
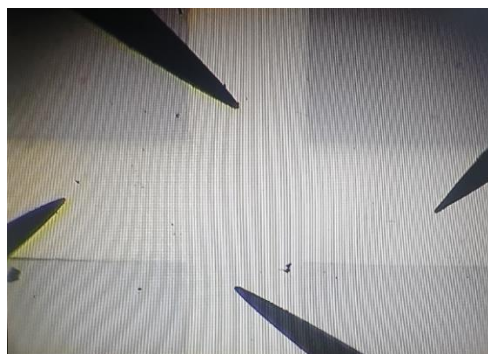

Figure 3.8: A photo of the spin Hall experiment configuration.

A Hall bar was sputtered in the HiTUS by placing a Hall bar mask designed for this project onto silicon substrate before deposition. The layers of the Hall bar consisted of 200 Å of $CoCr_{0.77}Fe_{0.91}Al_{0.83}$ and a capping layer of Pt with the thickness of 20 Å. Pt was chosen as the capping layer due to it being a heavy metal that exhibits strong spin-orbit coupling. The aim of this experiment was to investigate whether a spin Hall effect could be measured.
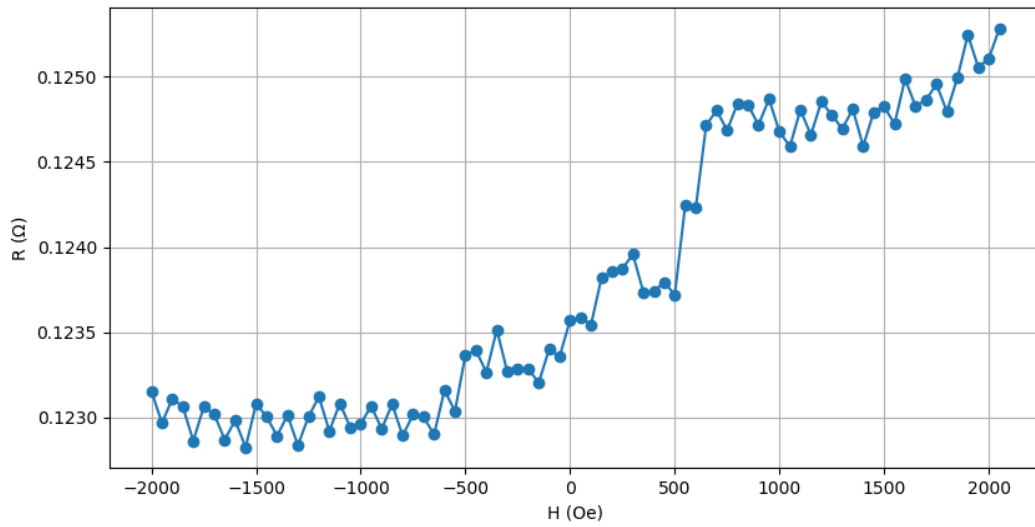
Figure 3.9: A graph of magnetic field applied vs spin Hall resistance.

Ohm's law was used to calculate the spin Hall voltage:

$$V_{SH} = I_c \times R_{SH} \tag{3.3}$$

where R_{SH} is the spin Hall resistance and I_c is the charge current. The V_{SH} was calculated to be 0.10 V. By using this value, it was possible to estimate the spin Hall angle using the following equation [65]:

$$\theta_{SH} = \frac{I_s}{I_e} \tag{3.4}$$

where I_s is the spin current. From this experiment, the spin Hall angle was estimated to be 0.019 (1.9%).

Previous papers give a range of values for the spin Hall of Pt, with most giving a spin Hall angle above 2 [65–67]. Even for papers where the experimental value

is below 0, no experimental results presented Pt to have a spin Hall angle of 0.019 [68]. Therefore, it is assumed that the spin Hall angle calculated is predominantly from CoCrFeAl.

 This is a relatively small spin Hall angle as an experiment conducted with Co-based Heusler alloys Co_2MnGa gave a spin Hall angle of $(19\pm4)\%$ [69]. A possible reason as to why the spin Hall angle is small in the sample could be because it is not perfectly ordered, therefore the spin gapless properties of CoCrFeAl has not been fully realised.

4. Conclusion

This research aimed to optimise CoCrFeAl for spin Hall device application.

CoCrFeAl thin films were grown using HiTUS sputtering onto Si substrates. Chemical analysis was conducted using SEM-EDX to investigate the properties of undoped CoCrFeAl thin film samples. Samples were found to be particularly deficient in Al and Cr. A range of different growth conditions were used in order to find the optimal growth conditions for CoCrFeAl samples.

XRD data was used for structural investigation of the crystal structure of undoped and doped samples. Undoped samples and doped samples with 1 Al peg, 1 Cr peg and 1 Al and 1 Cr pegs (1 peg doped samples) were observed to be amorphous in their as deposited state and when annealed at 300°C. A principle peak was observed about 44.5° in the as deposited and 1 peg doped samples at annealing temperature 400°C, with very little improvement in crystallinity at 500°C. This confirmed at least $A2$ ordering achieved in the CoCrFeAl samples. Phase segregation was detected in samples with 2 Al and 1 Cr pegs, 1 Al and 2 Cr pegs, and 2 Al and 1 Cr pegs (2 pegs doped samples). Whilst the stoichiometry did improve, it was difficult to investigate the crystallinity further because the poor quality of the θ-2θ XRD scan produced. This suggested that these 2 pegs doped samples may be less ordered than 1 peg doped samples.

VSM measurements were performed to investigate the magnetic properties of CoCrFeAl. It was found that all CoCrFeAl samples, undoped and doped, are magnetically soft with low coercivity, making CoCrFeAl ideal for data storage applications. VSM data revealed that doping has a significant impact of the saturation magnetisation of CoCrFeAl. This is seen in results ranging from approximately 100% of the theoretically calculated value of saturation magnetisation ($\sim$783 emu/cm^3) to 6% of the theoretically calculated value. The 2 doped samples showed different magnetic behaviour to undoped and 1 doped samples as they possess weak ferromagnetic behaviour in the as deposited state and at 300°C. This shows an excess of Al or Cr may lead to phase segregation.

Results from the spin Hall experiment showed that CoCrFeAl has a spin Hall angle (θ_{SH}) of 0.019 which confirmed that this Heusler alloy may have the

potential to work for spin Hall devices but more work is needed to optimise the crystal structure of CoCrFeAl in order to utilise the full potential of its spin gapless behaviour.

5. Further Work

Optimisation of CoCrFeAl posed a significant challenge. More in depth structural analysis of the crystal structure of CoCrFeAl thin film deposited by HiTUS sputtering is needed to optimise the growth conditions for spin Hall devices. This could be done by using microscopy or spectroscopy techniques such as transition electron microscopy (TEM) and Raman spectroscopy respectively. Using such technique would possibly make it easier to determine what is the typical crystal structure configuration for CoCrFeAl and how doping may affect it or lead to phase segregation and how it can be avoided.

Given that temperature has been shown to improve crystallinity and saturation magnetism in this study, annealing *in-situ* pre or post deposition may yield different results to the ones presented in this study such as improved disorder or different grain sizes.

This study serves as a starting point in investigating CoCrFeAl capability for application in spin Hall devices.

6. Reference

[1] W. Thomson, R. Soc. Proceedings of the Royal Society (1857).

[2] G. Binasch, P. Grünberg, F. Saurenbach, W. Zinn, Phys. Rev. B 39 (1989) 4828–4830.

[3] NobelPrize.Org (2007).

[4] N. Baibich, J. Broto, A. Fert, F. Nyugen Van Dau, P. Petroff, G. Eitenne, A. Creuzet, A. Friederich, J. Chazelas, Phys. Rev. Lett. 61 (1988) 2472–2475.

[5] N. Mott, R. Soc. 156 (1936).

[6] IBM, (2003).

[7] H. Gu, X. Zhang, H. Wei, Y. Huang, S. Wei, Z. Guo, Chem. Soc. Rev. 42 (2013).

[8] R. Ranjbar, Structural and Magnetic Properties for Bilayers of Cubic and Tetragonal Heusler Alloys, 2018.

[9] Des. Reuse (2020).

[10] G.E. Moore, 38 (1965).

[11] D. Yu, K. Yu, R. Tan, Clean. Responsible Consum. 1 (2020).

[12] C. Minke, M. Suermann, B. Bensmann, R. Hanke-Rauschenback, Int. J. Hydrog. Energy 46 (2021) 23581–23590.

[13] K. Elphick, W. Frost, M. Samiepour, T. Kubota, K. Takanashi, H. Sukegawa, S. Mitani, A. Hirohata, Sci. Technol. Adv. Mater. 22 (2021) 235–271.

[14] Rare Earth Elements—Critical Resources for High Technology, 2002.

[15] C. Felser, A. Hirohata, Heusler Alloys: Properties, Growth, Applications, Springer, Berlin, 2015.

[16] M. Dyakonov, V. Perel, JETP Lett. 13 (1971) 657.

[17] J.E. Hirsch, Phys. Rev. Lett. 83 (1999) 1834–1837.

[18] S. Zhang, Phys. Rev. Lett. 85 (2000) 393–396.

[19] J. Sinova, D. Culcer, Q. Niu, N.A. Sinitsyn, T. Jungwirth, A.H. MacDonald, Phys. Rev. Lett. 92 (2004) 126603.

[20] P. Das, J. Slawinska, I. Vobornik, J. Fujii, A. Regoutz, J. Kahk, D. Scanlon, B. Morgan, C. Mcguinness, E. Plekhanov, D. Sante, Y.-S. Huang, R.-S. Chen, G. Rossi, S. Picozzi, W. Branford, G. Panaccione, D. Payne, (2017).

[21] E. Hall, Am. J. Math. 2 (1879) 287–292.

[22] F. Heusler, Verh Dtsch Phys Ges 5 (1903).

[23] T. Graf, C. Felser, S.S.P. Parkin, Prog. Solid State Chem. 39 (2011) 1–50.

[24] S. Ghosh, S. Ghosh, Phys. Status Solidi B 256 (2019) 1900039.

[25] P. Cao, H. Zhao, S. Liu, F. Tian, Y. Wang, Phys. Lett. A 383 (2019) 125934.

[26] H.C. Kandpal, G.H. Fecher, C. Felser, J. Phys. Appl. Phys. 40 (2007) 1507.

[27] K. Buschow, P. Van Engen, J. Magn. Magn. Mater. 25 (1981) 90–96.

[28] H. van Leuken, R.A. de Groot, Phys. Rev. Lett. 74 (1995) 1171–1173.

[29] G.H. Fecher, S. Chadov, C. Felser, in: C. Felser, G.H. Fecher (Eds.), Spintron. Mater. Devices, Springer Netherlands, Dordrecht, 2013, pp. 115–165.

[30] I. Galanakis, P. Dederichs, N. Papanikolaou, Phys. Rev. B 66 (2002) 174429.

[31] J.C. Slater, J. Appl. Phys. 8 (1937) 385.

[32] L. Pauling, Phys. Rev. 54 (1938) 899–904.

[33] A. Kundu, S. Ghosh, R. Banerjee, S. Ghosh, B. Sanyal, Sci. Rep. 7 (2017).

[34] (n.d.).

[35] I. Galanakis, P.H. Dederichs, N. Papanikolaou, Phys. Rev. B 66 (2002) 134428.

[36]   S. Ishida, S. Fujii, S. Kashiwagi, S. Asano, J. Phys. Soc. Jpn. 64 (1995) 2152–2157.

[37]   I. Galanakis, P. Mavropoulos, P.H. Dederichs, J. Phys. Appl. Phys. 39 (2006) 765.

[38]   S. Picozzi, A. Continenza, A.J. Freeman, Phys. Rev. B 69 (2004) 094423.

[39]   S. Wurmehl, G.H. Fecher, H.C. Kandpal, V. Ksenofontov, C. Felser, H.-J. Lin, J. Morais, Phys. Rev. B 72 (2005) 184434.

[40]   Y.V. Kudryavtsev, V.N. Uvarov, V.A. Oksenenko, Y.P. Lee, J.B. Kim, Y.H. Hyun, K.W. Kim, J.Y. Rhee, J. Dubowik, Phys. Rev. B 77 (2008) 195104.

[41]   S. Khmelevskyi, P. Mohn, J. Magn. Magn. Mater. 560 (2022) 169615.

[42]   Y. Miura, M. Shirai, K. Nagao, J. Appl. Phys. 99 (2006) 08J112.

[43]   M. Yamamoto, T. Marukame, T. Ishikawa, K. Matsuda, T. Uemura, M. Arita, J. Phys. Appl. Phys. 39 (2006) 824.

[44]   E.J. O'Sullivan, MAGNETIC TUNNEL JUNCTION-BASED MRAM AND RELATED PROCESSING ISSUES, IBM, 2005.

[45]   D. Rani, L. Bainsla, A. Alam, K.G. Suresh, J. Appl. Phys. 128 (2020) 220902.

[46]   Q. Gao, I. Opahle, H. Zhang, Phys. Rev. Mater. 3 (2019) 024410.

[47]   X. Wang, Z. Cheng, J. Wang, X.-L. Wang, G. Liu, J. Mater. Chem. C 4 (2016) 7176–7192.

[48]   K. Özdoğan, E. Şaşıoğlu, I. Galanakis, J. Appl. Phys. 113 (2013) 193903.

[49]   A. İyigör, Ş. Uğur, Philos. Mag. Lett. 94 (2014) 708–715.

[50]   G.Y. Gao, L. Hu, K.L. Yao, B. Luo, N. Liu, J. Alloys Compd. 551 (2013) 539–543.

[51]   G.Z. Xu, E.K. Liu, Y. Du, G.J. Li, G.D. Liu, W.H. Wang, G.H. Wu, Europhys. Lett. 102 (2013) 17007.

[52]   S. Tsujikawa, I. Shigeta, J. Gouchi, T. Kanomata, R.Y. Umetsu, Y. Uwatoko, M. Hiroi, IEEE Trans. Magn. 58 (2022) 1–5.

[53]   P. Kharel, W. Zhang, R. Skomski, S. Valloppilly, Y. Huh, R. Fuglsby, S. Gilbert, D.J. Sellmyer, J. Phys. Appl. Phys. 48 (2015) 245002.

[54]   L. Bainsla, A.I. Mallick, A.A. Coelho, A.K. Nigam, B.S.D.Ch.S. Varaprasad, Y.K. Takahashi, A. Alam, K.G. Suresh, K. Hono, J. Magn. Magn. Mater. 394 (2015) 82–86.

[55]   Z.X. Chen, Y. Sakuraba, K. Masuda, X.D. Xu, L.S.R. Kumara, H. Tajiri, Y. Kotani, V. Kushwaha, A. Perumal, K. Hono, Acta Mater. 232 (2022) 117958.

[56]   M. Vopsaroiu, M.J. Thwaites, S. Rand, P.J. Grundy, K. O'Grady, IEEE Trans. Magn. 40 (2004) 2443–2445.

[57]   PlasmaQuest, (n.d.).

[58]   M. Vopson, M. Thwaites, G. Fernandez, S. Lepadatu, K. grady, J. Optoelectron. Adv. Mater. 7 (2005).

[59]   K. Inaba, S. Kobayashi, K. Uehara, A. Okada, S. Reddy, T. Endo, Adv. Mater. Phys. Chem. 3 (2013) 72–89.

[60]   H. Wu, Structural and Magnetic Characterisation of Heusler Alloy Thin Films under Optimised Growth Condition for Spintronic Devices, Univeersity of York, 2018.

[61]   JSM-7800FPRIME Schottky Field Emiss. Scanning Electron Microsc. Prod. JEOL Ltd (n.d.).

[62]   P. Kinsler, Physics 2 (2020) 150–163.

[63]   F.E. Hoare, J.C. Matthews, J.C. Walling, Proc. R. Soc. Lond. Ser. Math. Phys. Sci. 216 (1953) 502–515.

[64]   X. Wang, Natl. Sci. Rev. 4 (2017) 252–257.

[65]   L. Liu, T. Moriyama, D.C. Ralph, R.A. Buhrman, Phys. Rev. Lett. 106 (2011) 036601.

[66]   M. Althammer, S. Meyer, H. Nakayama, M. Schreier, S. Altmannshofer, M. Weiler, H. Huebl, S. Geprägs, M. Opel, R. Gross, D. Meier, C. Klewe, T. Kuschel, J.-M. Schmalhorst, G. Reiss, L. Shen, A. Gupta, Y.-T. Chen, G.E.W. Bauer, E. Saitoh, S.T.B. Goennenwein, Phys. Rev. B 87 (2013) 224401.

[67]   H. Nakayama, M. Althammer, Y.-T. Chen, K. Uchida, Y. Kajiwara, D. Kikuchi, T. Ohtani, S. Geprägs, M. Opel, S. Takahashi, R. Gross, G.E.W. Bauer, S.T.B. Goennenwein, E. Saitoh, Phys. Rev. Lett. 110 (2013) 206601.

[68]   A. Hoffmann, IEEE Trans. Magn. 49 (2013) 5172–5193.

[69]   L. Leiva, S. Granville, Y. Zhang, S. Dushenko, E. Shigematsu, T. Shinjo, R. Ohshima, Y. Ando, M. Shiraishi, Phys. Rev. B 103 (2021) L041114.

Appendix

VSM plot of undoped CoCrFeAl samples
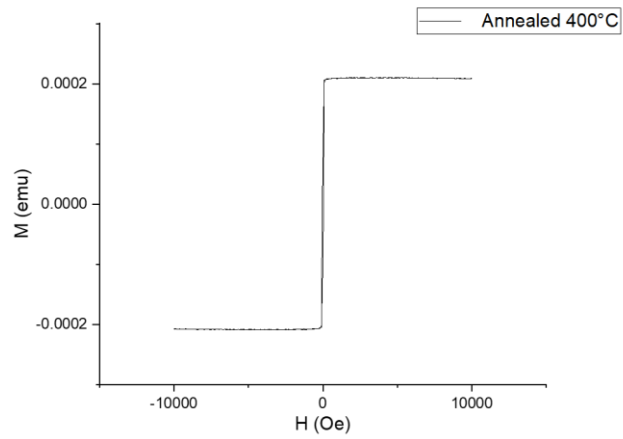
a)
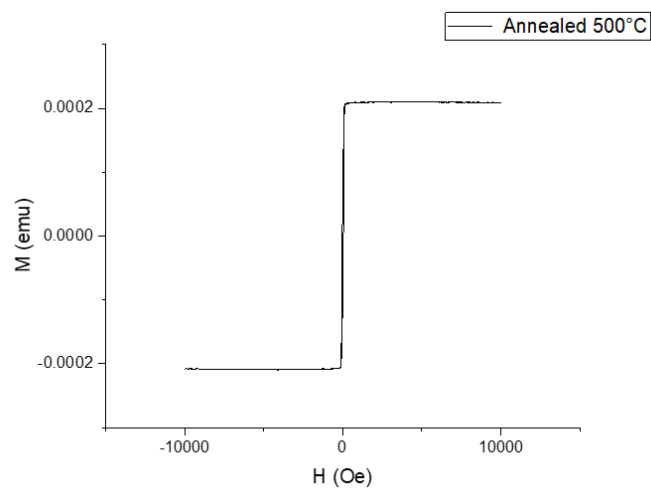
b)

Figure A1: VSM plot for undoped CoCrFeAl annealed at a) 400°C and b) 500°C. Both have a saturation magnetisation of approximately 444 emu/cm^3.
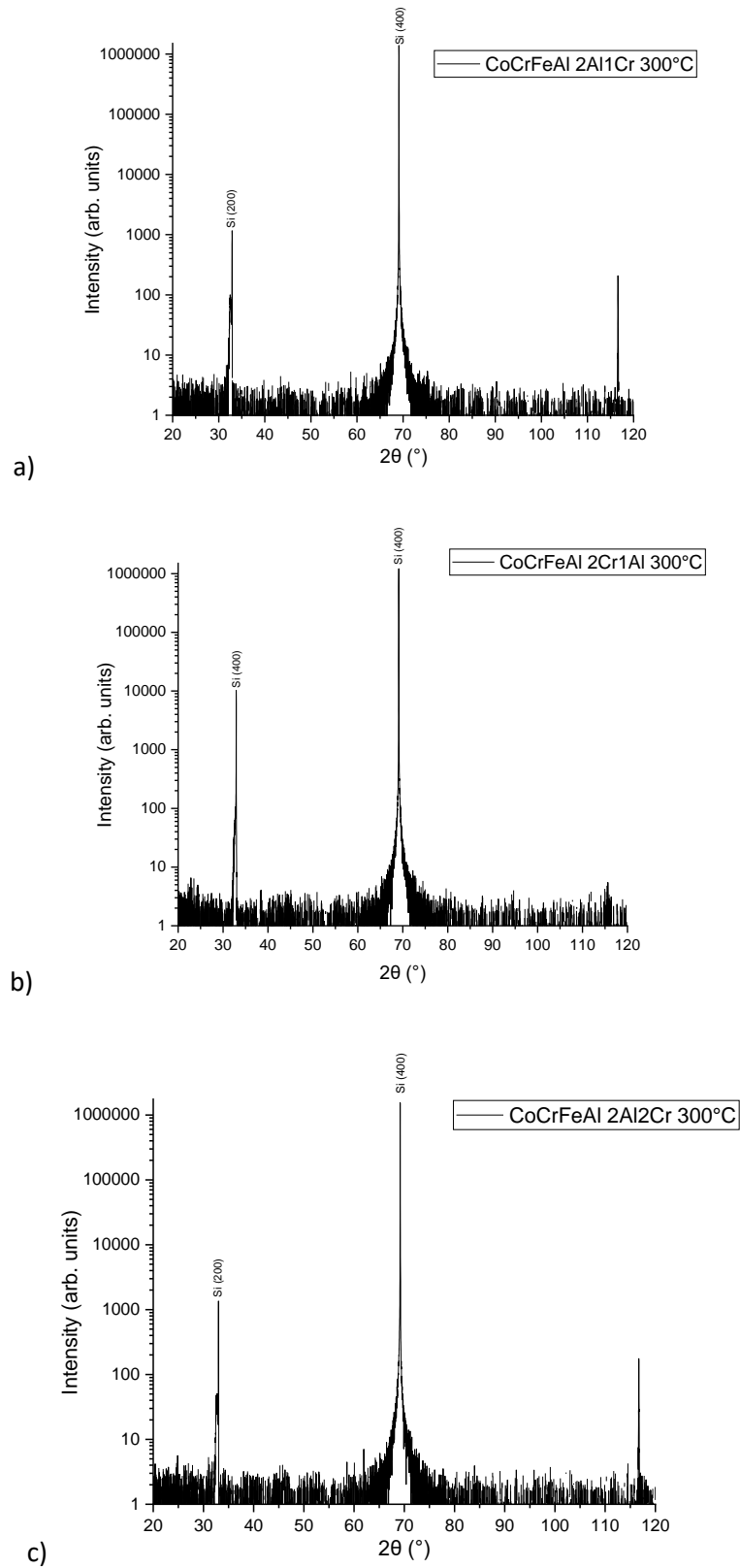
XRD theta-2theta scans of 2 doped samples

Figure A2: XRD ther02theta scans of CoCrFeAl samples annealed at 300°C with growing conditions of a) 2 Al and 1 Cr pegs b) 2 Cr and 1 Al pegs and c) 2 Al pegs and 2 Cr pegs.
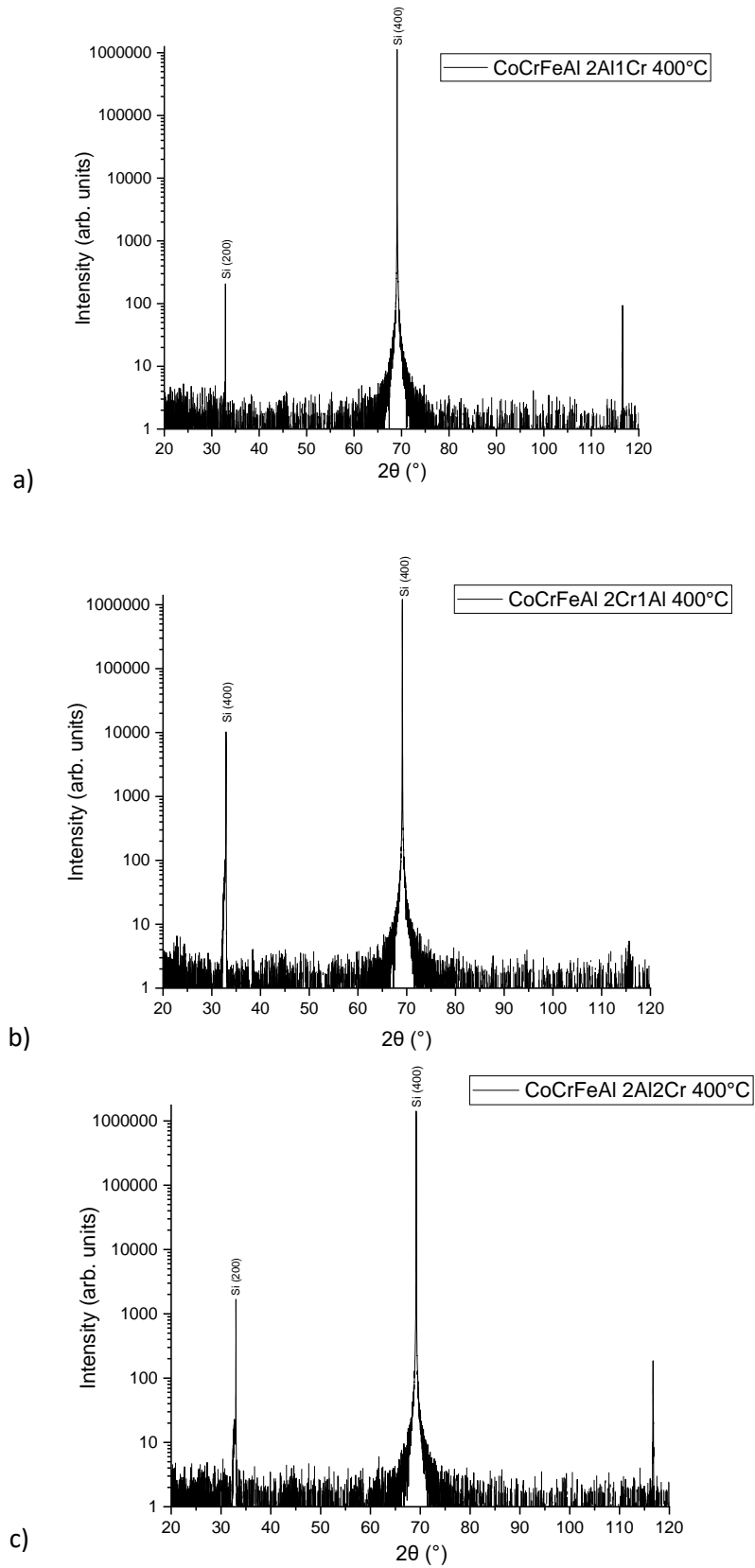
Figure A3: XRD ther02theta scans of CoCrFeAl samples annealed at 400°C with growing conditions of a) 2 Al and 1 Cr pegs b) 2 Cr and 1 Al pegs and c) 2 Al pegs and 2 Cr pegs.
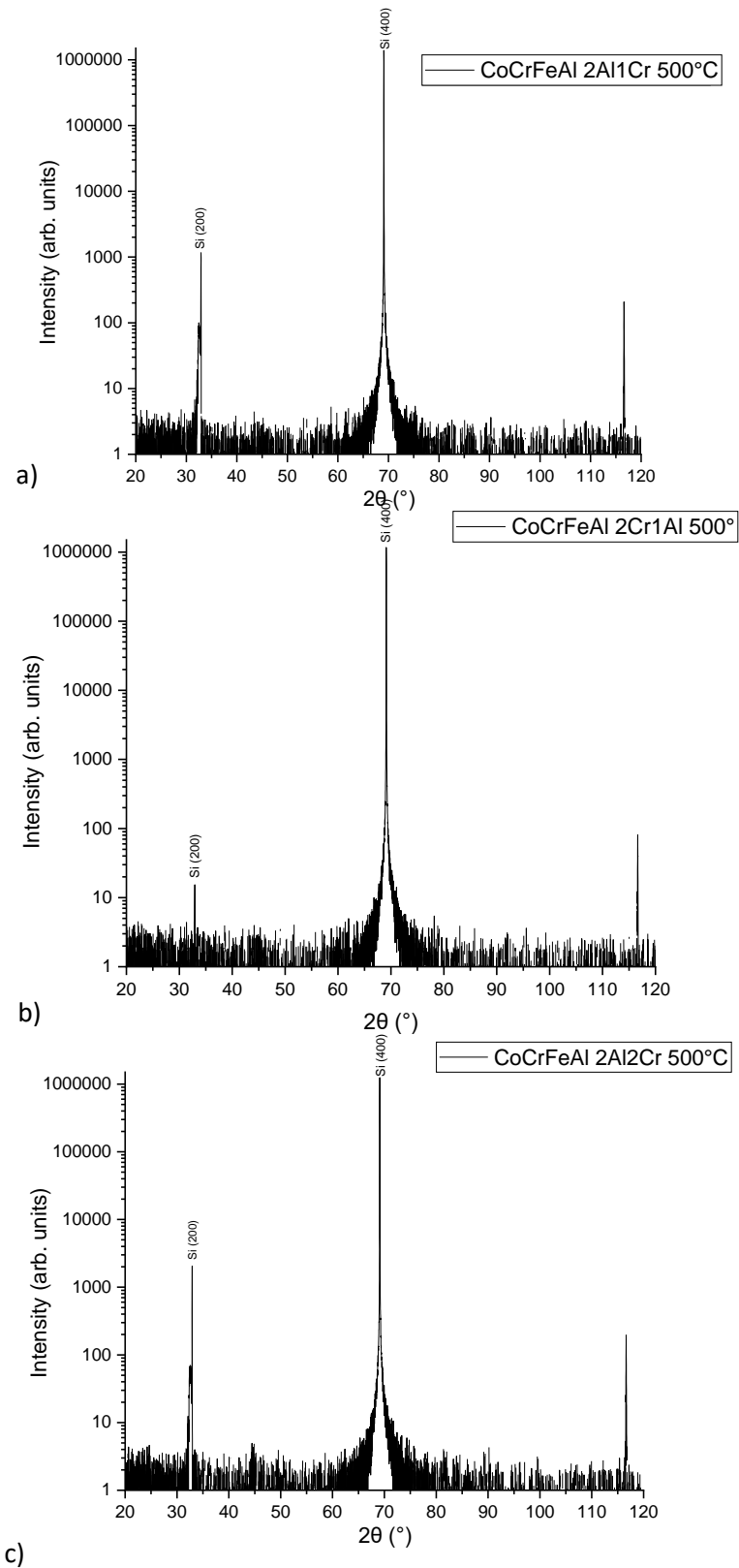
Figure A4: XRD theta-2theta scans of CoCrFeAl samples annealed at 500°C with growing conditions of a) 2 Al and 1 Cr pegs b) 2 Cr and 1 Al pegs and c) 2 Al and 2 Cr pegs.